Global scale magnetic field extrapolation in the solar corona using a Yin Yang grid

Dissertation

zur Erlangung des mathematisch-naturwissenschaftlichen Doktorgrades

"Doctor rerum naturalium"

der Georg-August-Universität Göttingen

im Promotionsstudiengang Physik

der Georg-August University School of Science (GAUSS)

vorgelegt von

Argyrios Sotirios Koumtzis

aus Thessaloniki, Greece

Göttingen, 2023

Betreuungsausschuss

Prof. Dr. Hardi Peter
Max-Planck-Institut für Sonnensystemforschung, Göttingen, Germany

Dr. Thomas Wiegelmann
Max-Planck-Institut für Sonnensystemforschung, Göttingen, Germany

Prof. Dr. Stefan Dreizler
Georg-August University School of Science (GAUSS), Göttingen, Germany

Mitglieder der Prüfungskommision

Referent: Prof. Dr. Hardi Peter
Max-Planck-Institut für Sonnensystemforschung, Göttingen, Germany

Korreferent: Prof. Dr. Stefan Dreizler
Georg-August University School of Science (GAUSS), Göttingen, Germany

Weitere Mitglieder der Prüfungskommission:

Prof. Dr. Sami Solanki
Max-Planck-Institut für Sonnensystemforschung, Göttingen, Germany

Prof. Dr. Jens Niemeyer
Georg-August University School of Science (GAUSS), Göttingen, Germany

PD Dr. Olga Shishkina
Max-Planck-Institut für Dynamik und Selbstorganisation

Prof. Dr. Wolfram Kollatschny
Georg-August University School of Science (GAUSS), Göttingen, Germany

Tag der mündlichen Prüfung:

Contents

Summary

The solar magnetic field significantly influences and structures the solar coronal plasma as magnetic forces are the dominant forces within the solar corona. Therefore, an in-depth understanding of the phenomena that occur there requires the best possible description of the coronal magnetic field. Prominent instances of such phenomena include solar flares, which are abrupt discharges of electromagnetic energy observed through the whole electromagnetic spectrum. Solar flares can unleash as much energy as a billion atomic bombs in just a matter of minutes. Other crucial phenomena are coronal mass ejections (CMEs), colossal solar storms that explosively move vast clouds of hot, magnetized plasma-comprising electrons, protons, and atomic nuclei into interplanetary space at speeds that can exceed several million miles per hour. Lastly, there's the solar wind, a continuous outflow of charged particles, primarily electrons and protons. These particles, streaming along the Sun's highly dynamic magnetic field, permeate the solar system at speeds ranging from 250 to 750 kilometers per second. These phenomena serve as the primary engines behind space weather. They lead to beautiful displays such as the auroras we observe on Earth caused by solar particles colliding with Earth's atmospheric gases. However, these solar events can also provoke catastrophic consequences. These include disruptions to telecommunications and satellite operations, and profound effects on critical infrastructure such as power grids. When severe, these disruptions can lead to extensive power outages and satellite failures, underscoring the importance of monitoring and understanding these dynamic solar processes.

Although direct, regular measurements of the coronal magnetic field aren't accessible yet, we can study its structure and dynamics by extrapolating the photospheric vector-field measurements into the corona. This thesis particularly discusses global coronal structures, typically modeled using spherical grids because of the spherical geometry present on the Sun and synoptic vector magnetograms as the boundary conditions.

We have developed a new numerical code that facilitates nonlinear force-free magnetic-field extrapolations in spherical geometry. This code is based on a well-tested optimization principle that has been successfully applied to a Cartesian grid and a single spherical finite-difference grid. This is the first instance where the algorithm can reconstruct the magnetic field across the entire corona, encompassing the polar regions.

The previous versions of this spherical code experienced numerical inefficiencies due to the convergence of these grids at the solar polar regions. The new code has incorporated the so-called Yin-Yang overhead grid, which effectively tackles this issue. As a result, both the speed and accuracy of the optimization algorithm have been enhanced relative to the earlier versions. We validate our new code using a widely recognized semi-analytical model, the Low and Lou solution, which is often used as a standard to test nonlinear force-free extrapolation codes. We then use vector synoptic magnetograms

provided by the Helioseismic Magnetic Imager (HMI) on board the Solar Dynamics Observatory (SDO) as a boundary condition for our model and reconstruct the global coronal magnetic field. We chose to study the performance of our model during two periods of significantly different solar activity: one during solar maximum activity and one during solar minimum activity. We compare the resulting field lines with relevant observations to further investigate the quality of our solutions. We then discuss the possible applications of our code and what research questions we could address with this newly developed tool.

1 Introduction

1.1 The solar structure

When looking at the Sun, although it is not recommended to look directly at it, our eyes register the photons within the visible electromagnetic spectrum that manage to travel through interplanetary space to Earth's surface. The layer of the Sun that is visible to our naked eye is called the photosphere. The Sun is divided into several spherical layers. Below the photosphere is the convection zone, which extends from 70% of the solar radius to the solar surface. The temperature difference between the inner and outer boundaries is such that it provides the conditions for the existence of thermal currents. This is the part of the Sun where large and small-scale flows generate the solar magnetic field before it surfaces to the photosphere. See the review article by Featherstone and Hindman (2020) for a more detailed discussion on the convection zone.

Going even deeper into the solar structure, we find the radiation zone, which extends from the outer boundary of the convection zone to around 20% of the solar radius. The temperature in the radiation zone is 1.5 to 2 million K and consequently the plasma is highly ionized. Therefore, there are many free electrons that scatter photons. This high density of scatterers is responsible for the long time (thousands to millions of years) it takes photons to travel through the radiation region (see Gough 2017, for details). The core is the central region of the Sun, extending from the solar center to about 20 % of the solar radius. It is an incredibly hot and dense region, with temperatures around from 15 million Kelvin and densities around 150 times that of water. The high temperature and pressure in the core allow for nuclear fusion to occur, which is the process of combining atomic nuclei to form heavier elements and releasing energy during the process.

In the core of the Sun, nuclear fusion primarily involves the fusion of four hydrogen nuclei, or protons, into a single helium nucleus. This process releases an enormous amount of energy in the form of gamma rays, which then gradually convert into other forms of energy as they move outwards through the Sun's layers.

The process of fusion in the core is facilitated by the high temperatures and densities present there. At these extreme conditions, the kinetic energy of the protons is high enough to overcome their mutual electrostatic repulsion and get close enough for the strong nuclear force to bind them together. This results in the formation of a helium nucleus, two neutrinos, and an enormous amount of energy.

However, nuclear fusion is not a simple process and requires a delicate balance between the temperature, density, and composition of the material in the core. If the temperature and pressure are too low, fusion reactions will not occur efficiently enough to sustain the Sun's energy output. Conversely, if the temperature and pressure are too high,

the core will expand and cool, reducing the rate of fusion and leading to a decrease in energy production. This process, which is an instance of nuclear fusion, is what "makes the star alive" in the sense that it provides the thermal energy that sets into motion the solar radiation, the thermal currents, and defines the parameters of the stellar structure.

The layers above the photosphere are not usually visible with the naked eye because the number of photons is a lot lower than the one coming from the photosphere, and we cannot distinguish the lower luminosity source because of its proximity to a much brighter one. One instance when the solar atmosphere is visible is during a total solar eclipse. The solar atmosphere includes four different regions: the photosphere, the chromosphere, the transition region, and the corona. The chromosphere, when observed, is typically shown with a red color because of the strong emission in the Hα spectral line. The word chromosphere (from the Greek chroma=color) literally means the sphere of color.

The height of the chromosphere varies between 3 000 to 5 000 kilometers, with a density that drops exponentially from $2 \times 10^{-4}\ kg/m^3$ to $1.6 \times 10^{-11}\ kg/m^3$, and a temperature that also decreases from 6 000 K to 3 800 K. The chromosphere is a region of the Sun where different dynamic phenomena are observed, such as plunges, spicules, cool loops, and chromospheric oscillations. See Klimchuk (2019) for a discussion about the structure and dynamics of the chromosphere.

Above the chromosphere, the next solar region is the transition region, a region where the physical characteristics of the solar atmosphere change dramatically in a very short distance when going from the chromosphere to the solar corona, which is the outermost layer of the solar atmosphere. Below the transition region, the structure of the Sun is defined by the gravitational forces in a way that makes it possible to separate into different layers. Above the transition region, the electromagnetic forces are dominant, increasing the complexity of the structure and dynamics.

Below the transition region, the ionization degree of helium molecules is relatively low, resulting in effective electromagnetic emission, while above the transition region, the helium is entirely ionized. When the helium molecules are fully ionized, they have no electrons and are not able to cool down using the electron transition mechanism. Therefore, above the transition region, the material remains orders of magnitude hotter.

Below the transition region, the spectral lines that are formed belong to the visible, infrared, and close to the ultraviolet range, while above the transition region, the lines are found in the extreme ultraviolet, hard and soft X-rays. The radiative transfer within the transition region is a highly complex problem due to the contribution of all the different physical processes that interplay in such a small spatial scale. Tian (2018) includes a great overview of the physics of the transition region.

The outermost region of the solar atmosphere is the solar corona. The dynamics and structure of the solar corona are dominated by the presence of the magnetic field, as the magnetic forces are stronger than all other forces. A quantity that is generally used to express the dominance of the magnetic forces is the plasma β, defined as

$$\beta = \frac{p}{B^2/2\mu_0}, \tag{1.1}$$

where p is the gas pressure, B is the magnetic field, and μ_0 is the vacuum permeability. By definition, when the plasma β is well below unity, the magnetic forces play the most important role in the plasma dynamics. As shown in Gary (2001), β is below unity in the

solar corona below about 2.5 solar radii.

The plasma in the corona is much hotter than the rest of the atmosphere, with temperatures ranging from 1 to 3 million Kelvin, which is about 3 orders of magnitude hotter than the photosphere. This is counterintuitive, as one would expect the temperature to drop monotonically with respect to distance from the heat source, which is the case for the solar interior. However, in the solar atmosphere, the magnetic field effects make the dynamics more complicated. This paradox is known as the coronal heating problem and is one of the open problems in solar and stellar astrophysics.

There are different mechanisms that could potentially explain how energy is transported into the corona. Two of the most supported ones by the scientific community are the alternating current heating models (AC) firstly proposed in Carlqvist (1977) and the direct current heating models (DC). The former is based on the observation that MHD waves observed in the corona (Tomczyk et al. 2007) can dissipate some of their energy in the form of heating, while the latter explains the heating with the existence of currents because of magnetic field motions (see Klimchuk (2015) for more details). Both of these proposed mechanisms show the importance of understanding the structure of the coronal magnetic field.

Other phenomena that take place in the corona are solar flares, sudden bursts of electromagnetic energy that can be observed from radio to hard X-rays. Very often, solar flares are accompanied by coronal mass ejections, gaseous explosions that could send coronal material to the interplanetary space, see Shibata and Magara (2011). The solar wind is a stream of charged particles, mainly protons and electrons, that flows continuously outward from the Sun in all directions. The high temperature of the coronal plasma, which can reach up to several million degrees, causes particles to escape the sun's gravitational field and form the solar wind. The structure of the coronal magnetic field strongly influences the solar wind, as the charged particles are guided along the magnetic field lines. The solar wind can have a significant impact on the Earth's environment, affecting our planet's magnetic field and causing auroras, as well as posing a potential hazard to spacecraft and communication systems. Understanding the solar wind and its variability is therefore an important area of research in solar physics. For a detailed discussion on the solar wind see Cranmer (2019). The content presented in this section can be found in Stix (2004).

1.2   Different coronal field extrapolation methods

In Section 1.1, the crucial role of the magnetic field in modeling the solar corona is discussed. In regions where the magnetic forces dominate the behavior of the plasma, such as in the corona, the physical phenomena are primarily of electromagnetic nature. Therefore, for accurate modeling of the phenomena in the solar corona, a precise and comprehensive description of the magnetic field is of utmost importance. Unfortunately, measuring the coronal magnetic field is really challenging. In Liu and Lin (2008) the authors attempted to compare directly measured magnetic field in the corona with potential field extrapolation. It is emphasized that this method is subject to various limitations such as the uncertainty regarding the point of the coronal emission and the need to use empirical analytical models for the structure of the solar atmosphere. Measuring the magnetic field

Figure 1.1: Solar eclipse observed in Portland, USA, on August 21, 2017. Courtesy: Pradeep L. Chitta

in the corona poses a significant challenge.

Despite these limitations, this study provides valuable insights into the complexities of measuring the magnetic field in the corona. These limitations make this kind of measurements a difficult tool in both modeling and validating coronal magnetic field models. Measuring the magnetic field in the lower parts of the solar atmosphere is an easier task that has been successfully performed during the last decades, in 1960s for the photosphere by Babcock (1961) and in the 1970s by Svalgaard et al. (1978). Chromospheric measurements were also first performed in the eighties (Jones 1985). EUV observations, although they are not able to provide the strength of the magnetic field, they can reveal the 3D structure of coronal loops and thus the direction of the magnetic-field vectors. A 3D reconstruction is possible when there are available observations from multiple points that can be used to look into a particular structure. For example, a stereoscopic method presented in Wiegelmann and Neukirch (2002) can be used to reconstruct the 3D geometry of loops in active regions. The basic assumption that enables the use of the EUV images for tracking magnetic loops is the fact that because of the low plasma β the plasma particles are guided along the magnetic field lines. As the thermal conductivity is much higher along the field lines and temperature gradients are higher perpendicular to them the plasma is confined within a loop. Consequently the emitting plasma on the loop outlines the magnetic field lines. The temperature range of the plasma within a coronal loop (10^6 K – 10^7 K) is such that they emit in the extreme ultraviolet part of the electromagnetic spectrum. By definition the magnetic field is parallel to the field lines at any given point so the geometry of the loops provides us with the direction of the coronal magnetic field.

The difficulties present in directly measuring the coronal magnetic field make the use of computational methods the only available option for studying the its structure. These computational reconstructions extrapolate the magnetic field measurements from either the photosphere or the chromosphere where they can be more accurately performed.

These numerical methods are generally called coronal magnetic field extrapolations. Every extrapolation method requires a set of assumptions for the description of the plasma in the solar corona. These assumptions lead to a system of partial differential equations, which have to be solved with adequate boundary conditions to reconstruct the coronal magnetic field structure in 3D.

There is a great variety of different methods ranging from the most involved ones like full magneto-hydro-dynamics (MHD) simulations where the full system of MHD is numerically solved (Feng et al. 2012, Lionello et al. 2014, Feng et al. 2021) to the simplest potential field extrapolation methods, where the working hypothesis is that there are no currents within the coronal volume (Schatten et al. 1969, Tóth et al. 2011). It is obvious that these models differ drastically in their complexity, the level of detail captured in their output solution and their needs for computational resources. Potential field models are easy to apply, but they do not perform well in describing the field in the low corona where the structure of the magnetic field is affected by currents within the coronal volume.

1.2.1 From MHD models to potential field extrapolations

Magneto-hydro-dynamics is the theoretical framework that describes the interactions of a magnetized fluid with a magnetic field. The MHD equations are:

$$\text{Continuity Equation:} \quad \frac{\partial \rho}{\partial t} + \nabla \cdot (\rho \mathbf{v}) = 0 \tag{1.2}$$

$$\text{Momentum Equation:} \quad \frac{\partial (\rho \mathbf{v})}{\partial t} + \nabla \cdot (\rho \mathbf{v} \mathbf{v} + p\mathbf{I} - \mathbf{B}\mathbf{B}) = \rho \mathbf{g} \tag{1.3}$$

$$\text{Induction Equation:} \quad \frac{\partial \mathbf{B}}{\partial t} = \nabla \times (\mathbf{v} \times \mathbf{B}) + \eta \nabla^2 \mathbf{B} \tag{1.4}$$

$$\text{Energy Equation:} \quad \frac{\partial e}{\partial t} + \nabla \cdot [(e + p)\mathbf{v} - (\mathbf{B} \cdot \mathbf{B})\mathbf{v} + \eta \mathbf{J} \times \mathbf{B}] = \rho \mathbf{g} \cdot \mathbf{v} \tag{1.5}$$

The symbols in these equations represent the following physical quantities:
ρ: mass density of the fluid
$\mathbf{v}$: fluid velocity vector
p: thermal pressure
$\mathbf{B}$: magnetic field vector
$\mathbf{I}$: identity matrix
$\mathbf{g}$: gravitational acceleration vector
η: magnetic diffusivity (resistivity)
$\mathbf{J}$: electric current density vector
e: total energy density, including kinetic, thermal, and magnetic components.
These equations are the main components of magnetohydrodynamics. The continuity equation represents the conservation of mass and the momentum equation the conservation of momentum (Navier-Stokes equation). The induction equation describes the evolution of the magnetic field while the energy equation represents the conservation of energy.

It is worth noting that in certain situations, additional forces may need to be included in the momentum equation. For instance, when working in a rotating frame of reference, as stars are, non-Newtonian forces such as centrifugal force and Coriolis force may become significant compared to other forces in the system.

The MHD approximation can be applied to study the phenomena in the solar corona as the mean free path of the particles comprising the plasma in the corona is significantly lower than the characteristic length scales present on the structures to be studied. For a detailed discussion for why this is a valid condition we refer to Petrie (2000) and for comparing with other theories that can be used to describe plasma-like kinetic theory see Marsch (2006).

The MHD models need to be provided with a set of initial conditions for all of the variables the MHD differential equations are solved for, including the scalar quantities (plasma pressure and the plasma density) and the vector quantities (plasma velocity and magnetic field). The uncertainty in estimating/measuring these quantities is a factor that affects the quality of their output solutions. The density and pressure profiles are often taken by assuming hydrostatic equilibrium while the magnetic fields are approximated by one of the simpler methods discussed below. Some models also include additional forces in the momentum equation like the gravitational force and forces caused by the solar rotation (centrifugal force and Coriolis force). The contribution of non-magnetic forces becomes important when studying the solar corona outside of the source surface where the plasma β is increasing again and thus their contribution is becoming significant compared to the magnitude of the magnetic force (Feng et al. 2012). The advantage of these models is that because their output is not limited to the magnetic field, all their output plasma parameters can be used to create synthetic images that can then be compared with observations in order to assess the quality of the reconstruction (Feng et al. 2012, 2021). A special class of MHD models is the stationary MHD models (Wiegelmann et al. 2020). The basic difference here is that the corona is approximated to be in a equilibrium state therefore all time-dependent terms in the MHD equations are zero. For stationary MHD equilibria the plasma velocity is not zero, but they consider the solar wind on open magnetic field lines. A further simplification are the magneto-hydro-static (MHS) models, which do not consider plasma flows. The MHS equations are given by

$$\frac{1}{4\pi}(\nabla \times \mathbf{B}) \times \mathbf{B} - \nabla p - \rho \nabla \Phi \;=\; 0, \qquad (1.6)$$

$$\nabla \cdot \mathbf{B} \;=\; 0. \qquad (1.7)$$

In equation 1.6, p and ρ are the plasma pressure and density respectively, and Φ is the gravity potential. For the MHS system to be complete, we need to connect density and pressure with temperature using an equation of state.

$$p = \rho k_B T / m, \qquad (1.8)$$

where T is the plasma temperature, k_B is the Boltzmann constant, and m the mean molecular mass of the gas particles.

In both cases (stationary MHD and MHS) the corona is described by going through a series of quasi-static states. This assumption is reasonable when the time difference between two consecutive states is smaller than the Alfvén time which is the characteristic time that the information needs to propagate within the corona (see Aschwanden 2005). For a detailed discussion on MHS methods see the review article by Zhu et al. (2022). The next even simpler modeling approach to model the coronal magnetic field is the nonlinear force-free field (NLFFF) approximation. When one neglects pressure gradients

and gravity terms then the system of equations is reduced to the vanishing Lorentz force equation

$$\vec{j} \times \vec{B} = 0 \tag{1.9}$$

and the divergence free condition 1.7. From 1.9 it is obvious that the magnetic field should either be parallel or anti-parallel to the electric current or that the current should be zero. Therefore, we can write the following equation as

$$\nabla \times \vec{B} = \alpha \vec{B}. \tag{1.10}$$

The quantity α is generally a function of the spatial coordinates. When combining 1.7 with 1.10

$$\vec{B} \cdot \nabla \alpha = 0 \tag{1.11}$$

For equation 1.11 we can deduce that α can take different values only when moving perpendicular to the field lines thus it is constant along each field line. When α is different for each field line then the extrapolation is called nonlinear force-free extrapolation. When α is chosen to be constant for the whole computational domain then this is the case of linear force-free extrapolation, and finally when $\alpha = 0$ we have the potential field extrapolation.

1.2.1.1 Nonlinear force-free models

The main argument for using the force-free approach is that as mentioned in section 1.1 the plasma β is two to four orders of magnitudes lower than unity within the solar corona and especially above the active regions. The magnetic forces drive all the charged particles to follow their geometry. The validity of this assumption is shown in Wiegelmann et al. (2020) where although the model is solving the stationary MHD equations the field does not deviate significantly by the nonlinear force-free solution. Reconstructing nonlinear force-free coronal magnetic fields is not a trivial task. For one, the field on the photosphere is not force-free in fact, the plasma β is close to unity which practically means that the gas pressure cannot be neglected. Therefore, one of the difficulties in performing force-free extrapolations is that the magnetic field used as a boundary condition for the computational models could be inconsistent with the force-free condition. An important remark here is that, as discussed in Wiegelmann and Sakurai (2021), although there are other forces (gravity and pressure gradient), it is possible that they cancel each other resulting in a boundary consistent with the force free condition. Another difficulty is the lack of vector data on the other boundaries of the computational domain. Ideally, we would like to have reliable measurements for all the 'box' boundaries but this is impossible because of our inability to accurately measure the magnetic field in the solar corona. One common solution to this problem is using even more simplified assumptions to fix the boundaries. For example, the application of the source surface condition (the field becomes purely radial at about 2.5 solar radii). This mimics the effect of the solar wind stretching and opening the magnetic field lines. Thus we get the condition $\vec{B}_\theta = \vec{B}_\phi = 0$ or the boundaries are taken from a potential field source surface (PFSS) extrapolation. The system of force-free equations 1.7 and 1.9 cannot be classified in the general types of partial differential equations (elliptical, parabolic, and hyperbolic). Therefore, its solution

requires special numerical methods. Some of the most successful methods for nonlinear force-free extrapolations are

- Grad-Rubin method (Sakurai 1981)

- Upward integration method (Wu et al. 1990)

- MHD relaxation method (Mikic and McClymont 1994, Valori et al. 2005, Inoue et al. 2014)

- Optimization method (Wheatland et al. 2000)

- Greens function method (Yan and Sakurai 2000)

- Force-free electrodynamics method (Contopoulos et al. 2011).

Another difficulty in developing force-free extrapolation methods is the lack of analytical solutions for nonlinear force-free magnetic field that could be used as test study cases to evaluate the performance of different numerical methods. There is however one semi-analytical solution designed by Low and Lou (1990) that is usually used as a benchmark solution. This solution can be used as a reference solution because although it does not have infinite accuracy, the fact that the 3D configuration depends on solving an ordinary differential equation and not a partial differential equation allows for solving with a very small iteration step thus achieving desired accuracy higher than the grid resolution. From all the methods listed above the ones that are widely used today are the MHD relaxation method, the Grad-Rubin method, and the Optimization method.

1.3   Potential field extrapolations

1.3.1   Mathematical foundation

When reconstructing the coronal magnetic field and the electric currents are completely neglected within the coronal volume, then the extrapolation method is called 'potential field extrapolation' because the magnetic field can be expressed as the gradient of a potential scalar field. As it is shown in Griffiths (2017), in chapter 6, the magnetic field is governed by the equation

$$\nabla \times \mathbf{B} = 0. \tag{1.12}$$

That subsequently means that the magnetic field is a curl-free vector field. By the Helmholtz decomposition theorem, any such vector field can be decomposed into the sum of a gradient field and a solenoidal field. The gradient field is of the form

$$\mathbf{B} = -\nabla \phi, \tag{1.13}$$

where ϕ is a scalar potential field. Taking the curl of both sides, we obtain

$$\nabla \times \mathbf{B} = \nabla \times (-\nabla \phi) = 0. \tag{1.14}$$

Therefore, the magnetic field can be expressed as the gradient of a scalar potential field ϕ. Taking the divergence of both sides of the equation $\mathbf{B} = -\nabla \phi$, we obtain

$$\nabla \cdot \mathbf{B} = -\nabla^2 \phi = 0 \tag{1.15}$$

which is the Laplace equation for the scalar potential field ϕ. Subsequently, solving the Laplace equation for the scalar field ϕ can then easily provide the magnetic field if we take its first gradient.

1.3.2   Different methods to solve the Laplace equation

The Laplace equation is a fundamental mathematical concept that is widely used to model various physical phenomena. Due to its versatility, numerous algorithms and methods have been developed over the years to solve the equation effectively.

- *Finite difference method*: The finite difference method involves approximating the Laplacian in the Laplace equation using a set of difference equations, which are then solved using linear algebra techniques. The method requires that the boundary conditions be specified at the grid points, and it is relatively simple to implement. Chapter 5 of the book covers the finite difference method. An example of the implementation of such a method on potential coronal field extrapolation is Altschuler and Newkirk Jr (1969b) and Han et al. (2018)

- *Finite element method*: The finite element method involves dividing the region of interest into smaller, simpler subregions, and then approximating the solution of the Laplace equation using a weighted sum of the solutions for each subregion. The method requires that the boundary conditions be specified on the boundaries of the subregions, and it can be used to solve problems with complex geometries. Chapter 10 of Gilat and Subramaniam (2014) covers the finite element method. This method is applied to the solar coronal field in McLaughlin (1989).

- *Boundary element method*: The boundary element method involves approximating the solution of the Laplace equation on the boundary of the region of interest, rather than on the interior. The method requires that the boundary conditions be specified on the boundary, and it can be used to solve problems with complex geometries. The method is relatively efficient, as it only requires the solution of linear algebraic equations, and it can be used to solve problems in two or three dimensions. Chapter 11 of Gilat and Subramaniam (2014) covers the boundary element method. In Glatzmaier (1987) the boundary element method is used for the reconstruction of the potential coronal magnetic field.

- *Method of moments*: The method of moments involves approximating the solution of the Laplace equation using a set of basis functions that satisfy the boundary conditions. The method requires that the boundary conditions be specified on the boundary of the region of interest, and it can be used to solve problems with complex geometries. The method is relatively efficient, as it only requires the solution of linear algebraic equations, and it can be used to solve problems in two or three dimensions. Chapter 12 of Gilat and Subramaniam (2014) covers the method of moments. This method is not yet used for potential field extrapolations in the solar corona.

- *Spectral methods*: The spectral methods involve approximating the solution of the Laplace equation using a sum of basis functions that are selected to match the problem geometry. The method requires that the boundary conditions can be specified on the boundary of the region of interest, and it can be used to solve problems with complex geometries. The method is relatively efficient, as it can produce accurate solutions using a relatively small number of basis functions, and it can be used to solve problems in two or three dimensions. Chapter 14 of Gilat and Subramaniam (2014) covers the spectral methods. In Altschuler and Newkirk Jr (1969a), the authors solve the Laplace equation in Cartesian geometry using a fast Fourier transformation (FFT). In Altschuler and Newkirk Jr (1969a), the authors use the spherical harmonics as the basis functions to calculate the potential magnetic field.

1.3.3 Spherical harmonics decomposition for solving the Laplace equation in spherical geometry

1.3.3.1 The 3D Laplace equation in spherical coordinates

The content of the subsubsection 1.3.3.1 is a summary of information included in chapter 3 of Griffiths (2017) The 3D Laplace equation in spherical coordinates is given by

$$\nabla^2 u = \frac{1}{r^2} \frac{\partial}{\partial r} \left(r^2 \frac{\partial u}{\partial r} \right) + \frac{1}{r^2 \sin\theta} \frac{\partial}{\partial \theta} \left(\sin\theta \frac{\partial u}{\partial \theta} \right) + \frac{1}{r^2 \sin^2\theta} \frac{\partial^2 u}{\partial \phi^2} = 0, \tag{1.16}$$

where u is the unknown function and ∇^2 is the Laplacian operator in spherical coordinates.

We can assume that the solution to the Laplace equation can be written as a product of three functions of the three independent variables, i.e.,

$$u(r, \theta, \phi) = R(r)Y(\theta)Z(\phi). \tag{1.17}$$

Using separation of variables in this context is justified because the Laplace equation is linear and homogeneous, meaning that any linear combination of solutions is also a solution. Therefore, if we can find a set of solutions to each of the separate ordinary differential equations, we can combine them to obtain a general solution to the Laplace equation. The assumption of separability simplifies the problem by reducing a partial differential equation to a set of ordinary differential equations, which are easier to solve.

By substituting 1.17 into the Laplace equation and separating the variables, we obtain three separate ordinary differential equations:

$$\frac{1}{R} \frac{d}{dr} \left(r^2 \frac{dR}{dr} \right) - \frac{\lambda^2}{r^2} = 0, \tag{1.18}$$

$$\frac{1}{Y} \left(\sin\theta \frac{d}{d\theta} \left(\sin\theta \frac{dY}{d\theta} \right) + \frac{\lambda^2}{\sin^2\theta} - \frac{m^2}{\sin^2\theta} \right) = 0, \tag{1.19}$$

$$\frac{d^2 Z}{d\phi^2} + \mu^2 Z = 0, \tag{1.20}$$

where λ, m, and μ are constants, which arise from the separation of variables.

The general solution to each of these equations is given by a linear combination of the associated Legendre functions $P_l^m(x)$ and $Q_l^m(x)$, and the spherical Bessel functions $j_l(x)$ and $y_l(x)$. The assumption of separability, in which we assume that the solution can be written as a product of functions of each independent variable, allows us to solve the 3D Laplace equation in spherical coordinates by solving the three separate ordinary differential equations and then combine the solutions using the principle of superposition.

1.3.4   Spherical harmonics expansion

When solving numerically the Laplace equation for the solar corona, the magnetic field at the inner boundary of the computational domain is specified based on accurate measurements from instruments. As a result, the boundary condition for this boundary is that the radial derivative of the scalar potential equals the magnetic field.

The steps for solving the Laplace equation on a sphere with a known gradient of the potential on the spherical boundary using spherical harmonics are:

- Start with the Laplace equation in spherical coordinates, which is given by

$$\nabla^2 u = \frac{1}{r^2}\frac{\partial}{\partial r}\left(r^2\frac{\partial u}{\partial r}\right) + \frac{1}{r^2\sin\theta}\frac{\partial}{\partial\theta}\left(\sin\theta\frac{\partial u}{\partial\theta}\right) + \frac{1}{r^2\sin^2\theta}\frac{\partial^2 u}{\partial\phi^2} = 0.$$

- Assume that the solution can be written as a sum of spherical harmonics, which are given by

$$Y_l^m(\theta,\phi) = (-1)^m\sqrt{\frac{2l+1}{4\pi}\frac{(l-m)!}{(l+m)!}}P_l^m(\cos\theta)e^{im\phi},$$

  where l and m are integers, with $l \geq |m|$, and P_l^m are the associated Legendre polynomials.

- Substitute the spherical harmonics into the Laplace equation and use the orthonormality property of the spherical harmonics to separate the equation into a set of equations for the coefficients:

$$\nabla^2 u = \sum_{l=0}^{\infty}\sum_{m=-l}^{l}c_{lm}\nabla^2 Y_l^m = \sum_{l=0}^{\infty}\sum_{m=-l}^{l}c_{lm}(-l(l+1))Y_l^m = 0,$$

  where c_{lm} are the expansion coefficients for the solution. This gives a set of equations for the coefficients

$$-l(l+1)c_{lm} = 0.$$

- Because $l(l+1) \geq 0$, the only solution to this equation is $c_{lm} = 0$ for all l and m except for $l = m = 0$. Therefore, the solution can be written as

$$u(r,\theta,\phi) = c_{00}Y_0^0(\theta,\phi),$$

  where c_{00} is a constant to be determined.

- Apply the boundary conditions to solve for the constant c_{00} and the expansion coefficients for the gradient of the potential. The boundary condition is given by

$$\frac{\partial u}{\partial r}(R, \theta, \phi) = g(\theta, \phi),$$

  where R is the radius of the sphere and $g(\theta, \phi)$ is the known gradient of the potential on the spherical boundary.

- Expand the gradient of the potential $g(\theta, \phi)$ in terms of the spherical harmonics

$$g(\theta, \phi) = \sum_{l=0}^{\infty} \sum_{m=-l}^{l} b_{lm} Y_l^m(\theta, \phi),$$

  where b_{lm} are the expansion coefficients for the gradient of the potential.

- Differentiate the solution expression with respect to r and substitute the expression for the solution $u(r, \theta, \phi)$ into the boundary condition, and equate it to the expansion of $g(\theta, \phi)$ in terms of the spherical harmonics

$$\frac{\partial u}{\partial r}(R, \theta, \phi) = c_{00} \frac{\partial}{\partial r} Y_0^0(R, \theta, \phi) = \sum_{l=0}^{\infty} \sum_{m=-l}^{l} b_{lm} \frac{\partial}{\partial r} Y_l^m(R, \theta, \phi).$$

- Use the derivative of the spherical harmonics with respect to r to isolate the constant c_{00}

$$c_{00} = \frac{1}{\frac{\partial}{\partial r} Y_0^0(R, \theta, \phi)} \sum_{l=0}^{\infty} \sum_{m=-l}^{l} b_{lm} \frac{\partial}{\partial r} Y_l^m(R, \theta, \phi).$$

- Substitute the expression for c_{00} into the solution expression:

$$u(r, \theta, \phi) = \frac{1}{\frac{\partial}{\partial r} Y_0^0(R, \theta, \phi)} \sum_{l=0}^{\infty} \sum_{m=-l}^{l} b_{lm} \frac{\partial}{\partial r} Y_l^m(r, \theta, \phi) Y_0^0(R, \theta, \phi).$$

- The solution can be evaluated at any point on the sphere using this expression, by substituting the values of r, θ, and ϕ for the desired point, and computing the sum over the expansion coefficients b_{lm}.

The expansion in terms of spherical harmonics provides a highly accurate representation of the solution and can be truncated after a finite number of terms to approximate the solution with any desired level of accuracy. The accuracy of the solution depends on the number of terms included in the expansion and can be improved by including more terms in the expansion.

1.4 Finite differences, finite volumes, and finite elements

1.4.1 Finite differences numerical methods

1.4.1.1 Introduction

According to LeVeque (2007), chapter 1, section "Introduction to Finite Differences", finite difference numerical methods are a class of numerical methods that are commonly used for approximating the solutions of differential equations. These methods rely on the idea of approximating the derivatives of a function at a point using the values of the function at nearby points.

The basic idea behind finite differences is to approximate the derivative of a function at a point by computing the difference between the function values at nearby points, divided by the distance between those points. Specifically, given a function $f(x)$ and a point x_0, we can approximate the derivative of $f(x)$ at x_0 using the formula

$$f'(x_0) \approx \frac{f(x_0 + h) - f(x_0)}{h},$$

where h is a small positive number (the 'step size') that determines the distance between the two points x_0 and $x_0 + h$. This approximation is called a 'forward difference' because it uses the value of f at x_0 and the value of f at a point slightly larger than x_0.

Similarly, we can approximate the derivative of $f(x)$ at x_0 using the formula:

$$f'(x_0) \approx \frac{f(x_0) - f(x_0 - h)}{h}.$$

This approximation is called a 'backward difference' because it uses the value of f at x_0 and the value of f at a point slightly smaller than x_0.

These two formulas are the basic building blocks of finite differences numerical methods. By combining them in various ways, we can approximate higher-order derivatives, solve differential equations, and perform a wide variety of other numerical calculations.

For example, we can use the forward difference formula to approximate the second derivative of $f(x)$ at x_0:

$$f''(x_0) \approx \frac{f'(x_0 + h) - f'(x_0)}{h}.$$

Substituting the first formula for $f'(x_0 + h)$ and simplifying, we get:

$$f''(x_0) \approx \frac{f(x_0 + 2h) - 2f(x_0 + h) + f(x_0)}{h^2}.$$

This formula is called a "centered difference" because it uses the values of f at three points ($x_0 - h$, x_0, $x_0 + h$) centered around x_0.

Finite difference methods can be used to approximate not only the first-order derivative but also higher-order derivatives, such as the second-order derivative. We will discuss three different approximations for the second-order derivative: central differences, forward differences, and backward differences.

1. Central differences:

The central difference method is a more accurate approximation of the second-order derivative than the forward or backward difference methods. The formula for the second-order central difference is derived by first approximating the first-order derivative using both the forward and backward difference formulas, and then combining them to find the second-order derivative. The formula for the second-order central difference is

$$f''(x_0) \approx \frac{f(x_0 + h) - 2f(x_0) + f(x_0 - h)}{h^2}.$$

This method uses the values of the function $f(x)$ at three points $(x_0 - h, x_0, x_0 + h)$ centered around x_0.

2. Forward differences:

The forward difference method for approximating the second-order derivative is based on the forward difference formula for the first-order derivative. To derive the formula, we first compute the forward difference for the first-order derivative at x_0 and $x_0 + h$, and then subtract them, resulting in

$$f''(x_0) \approx \frac{f'(x_0 + h) - f'(x_0)}{h}.$$

Next, we substitute the forward difference formula for the first-order derivatives, obtaining

$$f''(x_0) \approx \frac{f(x_0 + 2h) - f(x_0 + h) - (f(x_0 + h) - f(x_0))}{h^2}.$$

Simplifying the expression, we get

$$f''(x_0) \approx \frac{f(x_0 + 2h) - 2f(x_0 + h) + f(x_0)}{h^2}.$$

3. Backward differences:

Similarly, the backward difference method for approximating the second-order derivative is based on the backward difference formula for the first-order derivative. To derive the formula, we first compute the backward difference for the first-order derivative at x_0 and $x_0 - h$, and then subtract them, resulting in

$$f''(x_0) \approx \frac{f'(x_0) - f'(x_0 - h)}{h}.$$

Next, we substitute the backward difference formula for the first-order derivatives, obtaining

$$f''(x_0) \approx \frac{(f(x_0) - f(x_0 - h)) - (f(x_0 - h) - f(x_0 - 2h))}{h^2}.$$

Simplifying the expression, we get

$$f''(x_0) \approx \frac{f(x_0) - 2f(x_0 - h) + f(x_0 - 2h)}{h^2}.$$

These three methods for approximating the second-order derivative can be applied to various numerical calculations and can be easily extended to approximate higher-order derivatives. While central differences generally provide more accurate results, forward and backward differences can be useful in specific cases, such as when the function is not defined for certain values or when there are no data from both sides of the point where the derivative is to be calculated like the boundaries of a computational grid.

We can also use finite differences to solve differential equations by approximating the derivatives in the differential equation using finite differences. For example, consider the differential equation

$$y''(x) + p(x)y'(x) + q(x)y(x) = r(x).$$

We can approximate the second derivative $y''(x)$ using the centered difference formula, and approximate the first derivative $y'(x)$ using either the forward or backward difference formula, depending on the direction in which we are moving along the x-axis. We can then substitute these approximations into the differential equation and solve for $y(x)$ using standard numerical methods such as the Euler method, the Runge-Kutta method, or the shooting method.

Finite difference numerical methods have many advantages, including simplicity, flexibility, and ease of implementation. However, they also have some limitations, such as the fact that they can be prone to round-off errors, and the fact that they may not always converge to the true solution of a differential equation. Therefore, it is important to carefully analyze the accuracy and stability of finite difference numerical methods and choose the appropriate method for a given problem.

One important consideration when using finite differences is the choice of step size h. If h is too small, the approximation error will be small, but the round-off error may become significant. On the other hand, if h is too large, the approximation error will be large, and the approximation may be inaccurate. There are several techniques for choosing an appropriate value of h for a given problem. One common approach is to perform a convergence analysis, in which the approximation error is computed for a range of different values of h, and the value of h that produces the smallest error is chosen. Another approach is to use adaptive step size control, in which the value of h is adjusted dynamically during the calculation based on the behavior of the approximation error.

Despite their limitations, finite difference numerical methods remain an important tool for numerical analysis and scientific computing. They are widely used in a variety of applications, including physics, engineering, finance, and computer science, and they provide a powerful and flexible tool for approximating the solutions of differential equations and performing a wide range of other numerical calculations.

1.4.2   Solving partial differential equations using finite differences

As it is discussed in LeVeque (2007) in chapter 2 section "Finite differences for differential equations", one of the most important applications of finite differences is solving partial differential equations (PDEs). PDEs are equations that involve functions of several variables and their partial derivatives, and they arise in many areas of science and engineering, including physics, chemistry, and biology.

To solve a PDE using finite differences, we first discretize the domain of the PDE into a grid of points. We then use finite differences to approximate the partial derivatives of the function at each point on the grid. This results in a system of algebraic equations that can be solved numerically using standard methods.

The choice of grid spacing and the type of finite difference scheme used depend on the specific PDE being solved and the desired accuracy of the solution. For example, if the PDE is linear and homogeneous, a standard centered difference scheme with a small grid spacing may be sufficient to obtain an accurate solution. However, if the PDE is non-linear or has nonhomogeneous boundary conditions, more sophisticated finite difference schemes may be required to obtain an accurate solution.

In addition to the choice of finite difference scheme, the choice of boundary conditions is also important when solving PDEs using finite differences. The boundary conditions specify the behaviour of the solution at the edges of the domain, and they must be incorporated into the finite difference scheme in order to obtain an accurate solution.

Despite their complexity, finite difference numerical methods provide a powerful tool for solving a wide variety of PDEs. They are widely used in applications such as fluid dynamics, electromagnetism, and finance, and they continue to be an important area of research in numerical analysis and scientific computing.

1.4.3   Finite elements method

Another method to approximate solutions to partial differential equations (PDEs) is the finite element method (FEM). As it is explained in the book by Logan (2017), the method involves dividing the domain of the problem into smaller subdomains or elements, and approximating the solution within each element using simple functions called basis functions. These basis functions are chosen to match the behaviour of the true solution within each element.

The FEM works by converting the original PDE problem into a system of algebraic equations that can be solved using matrix techniques. This is done by defining a set of nodal values for the solution within each element, and then constructing a global system of equations by assembling the contributions from all the individual elements.

To solve the resulting system of equations, numerical techniques such as Gaussian elimination or iterative methods like successive over relaxation (Young 1950) and multi grid methods (Brandt 1977) can be used. Once the nodal values of the solution have been determined, the approximate solution can be reconstructed within each element using the basis functions. For a more detailed discussion on the mathematical foundation of the finite element method see Brenner and Scott (2007).

The FEM has many advantages over other numerical methods for solving PDEs, including its ability to handle complex geometries and boundary conditions, and its flexibility in choosing the approximation functions. It has a wide range of applications in engineering and science, including structural analysis (Courant 1943), fluid mechanics (Cardona et al. 2020), heat transfer (Dhiman and Gupta 2020), and electromagnetism (Guo et al. 2019).

1.4.4   Finite volume method

As it is discussed in Yu and Jin (2017), the finite volume method (FVM) is a numerical method for solving PDEs on a discretized domain. FVM is a special case of the finite element method (FEM) and shares many similarities with FEM. Both methods divide the domain into discrete elements and approximate the solution within each element using a set of basis functions. However, there are some fundamental differences between the two methods. In FVM, the computational domain is discretized into a set of control volumes or cells. The governing equations are then integrated over each control volume to obtain a discrete set of equations that can be solved numerically. The fluxes across the cell boundaries are computed using a numerical scheme, such as the upwind scheme or central differences, based on the values at the neighbouring cells. The value of the function is set to be constant within the volume element. This is different from the finite element method, which represents the solution by interpolating the function using a set of basis functions over each element and therefore the function can have different values within the same element.

One fundamental property of the FVM is that, by construction, conservation laws are satisfied. This ensures that the total quantity being transported, such as mass, momentum, or energy, is conserved across the domain. As a result of this conservation property, FVM is a suitable choice for physics simulations where the conservation of different quantities is of major importance. For example, FVM is commonly used in fluid dynamics simulations, where the conservation of mass, momentum, and energy are critical to the accuracy of the simulation. For a detailed presentation of different numerical implementations, algorithms and grid structures (see Guo et al. 2019). FVM is also used in other areas such as electromagnetic simulations, where the conservation of charge and energy is equally important (see Yang et al. 2021). In contrast, the FEM does not have the same conservation property as the FVM. While FEM is also a numerical method for PDEs, it approximates the solution by interpolating the function using a set of basis functions over each element. This means that FEM does not naturally conserve quantities and requires additional techniques to enforce conservation.

Another advantage of FVM is its ability to handle complex geometries and unstructured meshes. Because FVM only requires the computation of fluxes across element boundaries, it can be used with irregular meshes and complex geometries without the need for additional techniques such as mesh smoothing or mesh refinement.

1.4.5   Unstructured grid

According to Braess (2007), unstructured grids are defined as a type of numerical grids used in computational simulations that do not have a regular or uniform structure. Unlike structured grids, which consist of a regular array of identical cells or elements, unstructured grids are flexible and adaptable, allowing for more accurate simulations of complex geometries or physical phenomena.

Unstructured grids can be generated using various methods. The Delaunay triangulation was introduced by Boris Delaunay, a Russian mathematician. In Delaunay (1934), Delaunay was interested in finding the most efficient way to triangulate a set of points in the plane. He proved that the Delaunay triangulation, which he defined as the triangula-

tion that maximizes the minimum angle of the triangles, has several important properties, including that it is unique, and that it minimizes the number of triangles with obtuse angles. Nowadays, the Delaunay triangulation and methods based on it are some of the most commonly used techniques for generating unstructured grids in numerical simulations due to its simplicity, efficiency, and ability to adapt to complex geometries (see Bossavit 2003, Zhao et al. 2022). In Shewchuk (1996) advancing front techniques were introduced, which is another method for generating a mesh for numerical simulations of complex geometries. The method involves moving a front across the domain to be meshed and creating triangles as the front advances. The front starts with a set of seed points on the boundary of the domain and generates new points and triangles as it moves. The method can produce high-quality meshes with good geometric accuracy, but it can be computationally expensive compared to other mesh generation techniques. For a more detailed discussion of this method and a comparison with Delaunay triangulation see Loy et al. (2020).

The cells or elements in an unstructured grid can be triangles, quadrilaterals, in 2D, and tetrahedra, hexahedra in 3D. Other shapes can also be utilized depending on the nature of the specific problem (Huang et al. 2019) discusses in detail the advantages and disadvantages of the different shapes of the elements. Unstructured grids are often used in conjunction with numerical methods such as a finite element or finite volume methods, which are commonly used to solve differential equations, as discussed in the previous sections.

In general, unstructured grids are most useful when the geometry of the domain is complex or irregular, or when it changes over time. They can also be useful for adaptive mesh refinement and large-scale simulations. However, unstructured grids can be more difficult to generate and may require more computational resources than structured grids, so their use should be carefully considered based on the specific needs of the case in hand.

1.5 Finite differences spherical grids, challenges, and solutions

1.5.1 Finite difference spherical grids

The content of this section is based on Ruffert (2014). A finite difference spherical grid is a discretization of a spherical domain into a set of grid points, where the values of a solution are approximated by finite differences. This type of grid is commonly used to solve partial differential equations on a spherical domain, such as the Laplace or Poisson equations, and is particularly useful in geophysical and astrophysical applications such as seismology (Celli et al. 1999), astroseismology (Gough and Thompson 1988), and magnetospheric physics (Thanasoulis et al. 2020).

In a finite difference spherical grid, the sphere is divided into a set of points in the radial, polar, and azimuthal directions. The unit vectors associated with the polar radial and azimuthal directions, denoted $\hat{\mathbf{r}}$, $\hat{\theta}$, and $\hat{\phi}$, respectively, are defined in the same way as in spherical coordinates. These unit vectors are all perpendicular to each other, and point in the direction of increasing radius, polar and azimuthal angles, respectively. The unit vectors can be expressed in terms of a Cartesian frame of reference by using the

transformation equations

$$\hat{\mathbf{r}} = \left(\cos \phi \sin \theta, \sin \phi \sin \theta, \cos \theta \right),$$

$$\hat{\theta} = \left(\cos \phi \cos \theta, \sin \phi \cos \theta, -\sin \theta \right),$$

$$\hat{\phi} = \left(-\sin \phi, \cos \phi, 0 \right).$$

These equations express the unit vectors in terms of the Cartesian unit vectors $\hat{\mathbf{x}}$, $\hat{\mathbf{y}}$, and $\hat{\mathbf{z}}$, where $\hat{\mathbf{x}}$ points in the direction of increasing azimuthal angle, and $\hat{\mathbf{y}}$ and $\hat{\mathbf{z}}$ complete a right-handed coordinate system.

1.5.2 Convergence problem at the poles

One of the convergence problems associated with using a finite difference method on a spherical grid is the issue of grid convergence at the poles. The convergence of finite difference schemes can be adversely affected by the singular nature of the coordinate system at the poles of a spherical grid. This can lead to inaccurate solutions and numerical instabilities. In the field of coronal magnetic field extrapolations such problems are discussed in Usmanov (1996) and Wiegelmann (2007). Several techniques have been developed to handle the convergence problems at the poles. One of the commonly used methods is to apply a coordinate transformation that maps the original grid onto a new grid that is regular or quasi-regular near the poles. This means that the distance between grid points is more uniform, and the convergence issues can be mitigated. For example, in the context of modeling the Earth's atmosphere, the latitude-longitude grid can have convergence problems near the poles, where the meridians converge. To address this, a common approach is to use a coordinate transformation that maps the latitude-longitude grid onto a new grid that is regular near the poles, such as a polar stereographic projection. This can improve the accuracy and stability of the numerical method in these regions, allowing for more reliable simulations, see, e.g., Sun et al. (2011).

Another approach is to use a staggered grid, as done in Williamson and Drake (2003), where the variables are defined at different points in the grid, rather than at the same points. This can help to reduce the singularity problem and improve the accuracy of the numerical solution. A multi-grid approach can also be used. This method involves solving the problem on a sequence of grids with increasing resolution, starting from a coarse grid and moving towards a fine grid. At each level, a solution is calculated on the current grid and then interpolated to the next finer grid to obtain an initial guess for the solution. The solution is then refined on the finer grid using an iterative method, such as a relaxation method or a conjugate gradient method. The resulting solution on the finer grid is then interpolated back to the coarser grid to obtain an improved solution on the original grid. The multi-grid approach can help to improve the accuracy of the solution near the poles without requiring a large number of grid points. By starting from a coarse grid and progressively refining the solution on finer grids, the method can capture the relevant features of the solution at each level of resolution, while avoiding the need for excessively fine grids that would be computationally expensive. In the context of modeling the Earth's atmosphere or oceans, multi-grid methods have been widely used to handle convergence issues near the poles, where the meridians converge. These methods can help to improve

the accuracy and efficiency of numerical simulations and are commonly used in climate models and weather forecasting models as it is done in Skamarock and Klemp (1997).

Finally, another approach is to use a spectral method, as discussed in the section regarding potential field extrapolation. In that case, because the computation is done using the orthogonal base of functions the convergence of the spatial grid is not an issue. The grid convergence problem at the poles can also be avoided by using an unstructured grid (say triangles on the Sun's surface, tetrahedra in 3D) in combination with FEM or similar methods.

1.5.3 Yin-Yang grid as a solution to the convergence problem at the poles

The spherical Yin-Yang grid is a type of grid that is used for numerical simulations of problems on the surface of a sphere, such as weather forecasting or climate modeling. The Yin-Yang grid was introduced in Kageyama et al. (2004) as an elegant way to combine the benefits of a structured and unstructured grid.

The Yin-Yang grid consists of two identical, overlapping grids, each of which is based on a Cartesian coordinate system. One grid is oriented along the x, y, and z axes, while the other is oriented along the x, -y, and z axes. When the two grids are superimposed, they form a nearly spherical grid that has no singularities or abrupt changes in grid spacing. The grid is divided into four quadrants, which are labeled "Yin" and "Yang" based on their orientation in the Cartesian coordinate system. The computational spherical Yin-Yang grid is specifically designed for use in numerical simulations where the nature of the problem makes the use of a spherical grid an obvious choice. The grid is nearly isotropic, with nearly uniform spacing between grid points, and is free of singularities at the poles. It has several advantages over other types of grids, including its nearly uniform grid spacing, its ability to handle problems with steep gradients, and its compatibility with high-order numerical methods. The grid has been used in a variety of applications, including weather forecasting (Chen et al. 2013), climate modeling (Wang et al. 2014), astroseismology (Kpyl et al. 2010), and magnetic coronal field extrapolations (Jing et al. 2013).

1.6 Optimization algorithms

1.6.1 Introduction and definition

According to Nocedal and Wright (2006) and Pedregal (2004), chapter 1, optimization algorithms are mathematical procedures used to find the best solution or combination of parameters for a given problem. The goal of optimization is to find the optimal set of parameters that maximize or minimize a given objective function. Optimization algorithms are used in a wide range of applications, including engineering, economics, finance, logistics, and machine learning. In many real-world applications, finding the optimal solution can be very difficult or even impossible using traditional analytical methods. Optimization algorithms provide a way to search for the optimal solution efficiently and effectively,

often using numerical methods. Any optimization algorithm includes the following basic elements:

- *Objective function*: An objective function is a mathematical function that measures the quality of a solution. The goal of an optimization algorithm is to find the input values that minimize or maximize the objective function.

- *Decision variables*: Decision variables are the input values that can be adjusted to optimize the objective function. The decision variables can be continuous, discrete, or a combination of both.

- *Constraints*: Constraints are conditions that must be satisfied by the solution. Constraints can be expressed as mathematical equations or inequalities that restrict the feasible region of the decision variables.

- *Search space*: The search space is the set of all possible solutions to the optimization problem. The search space can be finite or infinite, discrete or continuous, and may or may not be bounded.

- *Iterative optimization process*: An optimization algorithm is a procedure that searches the search space to find the optimal solution. Optimization algorithms can be deterministic or stochastic and can be classified into different categories based on the search strategy and the solution representation.

- *Stopping criterion*: A stopping criterion is a condition that terminates the optimization algorithm when a certain convergence criterion is met. Stopping criteria can be based on the number of iterations, the change in the objective function, or other measures of convergence.

There are several types of optimization algorithms, for example gradient-based algorithms (Birkhoff and von Neumann 1946, Robbins and Monro 1951, Hestenes and Stiefel 1952) and metaheuristic algorithms (Holland 1975, Kirkpatrick et al. 1983, Kennedy and Eberhart 1995). Each type of algorithms has its own strengths and weaknesses, and the choice of an algorithm depends on the specific problem being solved and the computational resources available.

1.6.2 Gradient descent algorithm

1.6.2.1 Steepest descent

The work presented in this thesis is based on the gradient descent algorithm with a variable learning rate. The following section will provide a detailed explanation of the algorithm's basic idea and potential implementations. The "Numerical Optimization" book by Nocedal and Wright Nocedal and Wright (2006), in chapter 2, provides a comprehensive treatment of optimization algorithms, including the gradient descent algorithm. The gradient descent algorithm is an iterative optimization algorithm that is used to minimize an objective function. The basic idea is to start with an initial guess for the minimum and then iteratively update the guess using the negative gradient of the function at the current guess. The gradient represents the direction of the steepest ascent, so taking its negative

gives the direction of the steepest descent, which leads to the minimum. The algorithm continues to update the guess until a stopping criterion is met. The objective function is typically defined over a multivariate space, so the gradient descent algorithm is generalized to vector-valued functions. In this case, the gradient is replaced with the Jacobian matrix, which represents the matrix of partial derivatives of the objective function with respect to its variables.

The gradient of the objective function f(x) at the point x is given by

$$\begin{bmatrix} \frac{\partial f(x)}{\partial x_1} \\ \frac{\partial f(x)}{\partial x_2} \\ \vdots \\ \frac{\partial f(x)}{\partial x_n} \end{bmatrix}$$

The direction of the steepest descent at the point x is given by the negative gradient

$$d = -\nabla f(x).$$

The gradient descent algorithm updates the current point x_k by taking a step in the direction of the negative gradient, multiplied by a step size α_k

$$x_{k+1} = x_k + \alpha_k d.$$

The step size α_k is typically chosen using a line search algorithm to ensure that the algorithm is making sufficient progress in each iteration. One common approach is to choose α_k to satisfy the Armijo condition

$$f(x_k + \alpha_k d) \leq f(x_k) + c_1 \alpha_k \nabla f(x_k)^T d,$$

introduced in Armijo (1966), where c_1 is a constant between 0 and 1. The gradient descent algorithm continues to update the point x_k using the negative gradient direction until a stopping criterion is met, such as a maximum number of iterations or a minimum change in the objective function.

1.6.2.2 Stochastic gradient descent optimization method

Chapter 8 of "Numerical Optimization" by Nocedal and Wright (2006) provides a detailed introduction to stochastic gradient descent and its variants. The Stochastic Gradient Descent (SGD) algorithm is a popular optimization technique that is widely used in machine learning and other applications where the objective function is too large or too complex to be differentiated with respect to all its variables. The method was firstly proposed in Robbins and Monro (1951) in the context of finding the route to a nonlinear equation. The method is proven to be particularly effective even in cases where the traditional numerical methods struggle. In the same article, the authors discuss how this method can be implemented to find the minimum of a function. The modern stochastic gradient descent method and its variances are based on the work of this publication. The basic idea behind stochastic gradient descent is to approximate the objective function using a randomly-selected subset of the variables at each iteration. Rather than computing the gradient of

the objective function using the entire parameter set, SGD computes the gradient using a small subset of variables or even only one of them. This "stochastic" gradient is then used to update the variables of the optimization problem.

The advantage of stochastic gradient descent is that it can be much faster than steepest gradient descent, which computes the gradient using the entire parameter set at each iteration. Therefore, stochastic gradient descent can converge more quickly and more efficiently. However, attractive this method might look, there are still some challenges that need to be addressed. In particular, the stochastic gradient may be noisy or inaccurate, which can lead to slow convergence or even divergence of the algorithm. To address these issues, several variants of stochastic gradient descent have been developed, including:

Mini-batch gradient descent: This variant of SGD computes the gradient using a small batch of parameters, rather than a single one. This way, mini-batch SGD can reduce the noise in the gradient and improve convergence speed. It was introduced in Bottou (2010) and since then is one of the algorithms that are widely used in machine learning optimization.

Momentum-based methods: These methods use a weighted average of past gradients to update the parameters, which can help to smooth out the noise in the stochastic gradient and improve convergence. One of the most popular momentum-based methods is the Nesterov's accelerated gradient (see Nesterov 1983) which uses a lookahead gradient to improve convergence. Although in its original form, this method is using the full gradient of the objective function, it can be combined with the stochastic approach with even better results as it was introduced in Sutskever et al. (2013).

*Adaptive learning rate method*s: These methods adjust the learning rate based on the past gradients, which can help to ensure that the optimization process converges quickly and efficiently. One popular adaptive learning rate method is AdaGrad, which adapts the learning rate for each parameter based on the sum of the squares of the past gradients. This method was introduced in Duchi et al. (2011). The paper shows that AdaGrad can improve the convergence rate of stochastic optimization algorithms, particularly for problems with sparse gradients.

2 Developing a Yin-Yang code for force free full sphere extrapolation

The scientific content of chapter 2 was published in Koumtzis and Wiegelmann (2023).

2.1 Code description

2.1.1 Optimization code

Force-free magnetic-fields are defined by both a vanishing Lorentz force and a vanishing magnetic-field divergence. Therefore, they have to obey the following equations

$$(\nabla \times \vec{B}) \times \vec{B} = 0, \tag{2.1}$$
$$\nabla \cdot \vec{B} = 0. \tag{2.2}$$

One possibility to solve Equations 2.1 and 2.2 was proposed by Wheatland et al. (2000) through the minimization of a functional L. For the study of global coronal magnetic fields, we use a functional expressed in spherical geometry as introduced by Wiegelmann (2007) and defined as

$$L = \int_V \left[B^{-2} |(\nabla \times \vec{B}) \times \vec{B}|^2 + |\nabla \cdot \vec{B}|^2 \right] r^2 \sin\theta \, dr \, d\theta \, d\phi. \tag{2.3}$$

The definition of the functional (Equation 2.3) is such that $L = 0$ fulfils the requirement that the field is both force and divergence-free, because the quadratic form in the functional ensures that Equations 2.1 and 2.2 are satisfied for $L = 0$. The functional derivative of the functional leads to

$$\frac{\partial \vec{B}}{\partial t} = \mu \vec{F}, \tag{2.4}$$

where μ refers to a positive constant and the pseudo force $\vec{F}$ is defined as

$$\begin{aligned} \vec{F} &= \nabla \times (\vec{\Omega}_a \times \vec{B}) - \vec{\Omega}_a \times (\nabla \times \vec{B}) \\ &\quad + \nabla(\vec{\Omega}_b \cdot \vec{B}) - \vec{\Omega}_b(\nabla \cdot \vec{B}) + (\vec{\Omega}_a^2 + \vec{\Omega}_b^2) \, \vec{B} \end{aligned} \tag{2.5}$$

with

$$\vec{\Omega}_a = B^{-2} \left[(\nabla \times \vec{B}) \times \vec{B} \right] \tag{2.6}$$
$$\vec{\Omega}_b = B^{-2} \left[(\nabla \cdot \vec{B}) \, \vec{B} \right]. \tag{2.7}$$

A typical approach to solving nonlinear force-free equilibrium by minimizing Equation 2.3 is to use a potential field as the initial state, which is a special class of a force-free equilibrium. Potential fields are usually not consistent with the horizontal magnetic field measurements, which are used as the bottom boundary for our model. Subsequently when calculating the functional (Equation 2.3) after having replaced the bottom layer of the potential field with the observed field, there is a (large) deviation of force- and divergence freeness. The functional L is then minimized numerically by applying the iterative equation (Equation 2.4). For the tests performed in this study, we use synthetic synoptic vector magnetograms and generalize the implementation of our spherical optimization code for synoptic magnetograms as described by Tadesse et al. (2014).

2.1.2   Yin–Yang grid

When the optimization algorithm is implemented on a regular finite-difference spherical grid, there are some limitations when the computational domain extends towards the poles. Close to the polar regions, the spatial-grid converges, which means that the minimum distance between the grid points decreases. The iteration step scales with the square of the spatial grid resolution and consequently the number of iteration steps until L reaches its minimum increases dramatically. The dynamic time-step control in our previous spherical code (and also in the Cartesian code) decreases the time-step automatically when L does not monotonically decrease. Consequently, the time-step decreases by several orders of magnitude and the number of iterations steps until the convergence increases accordingly. Up to now, this limitation of the code was not significant for the application to currently available data, because the lack of reliable magnetic field measurements in solar polar regions did not allow accurate modeling of the coronal magnetic field above the poles in any case. Consequently, the computational domain was limited between 20 and 160 degrees in latitude to achieve a reasonable execution time. In the advent of polar magnetic field measurements from the *Solar Orbiter* mission, we implement the optimization code on a Yin–Yang grid to overcome the polar convergence issue. The Yin–Yang grid was introduced by Kageyama and Sato (2004) for geophysical applications. This overhead grid was to our knowledge first applied to solar applications by Jiang et al. (2012) who implemented a Yin–Yang grid in their CESE-MHD code to compute nonlinear force-free fields equilibria by MHD relaxation. A Yin-Yang grid was also implemented in the AMR-CESE-MHD code to study the global coronal evolution in a data-driven model by Feng et al. (2012). The Yin–Yang grid consists of two identical spherical grids. The first component of the grid is a regular spherical grid with some cutout regions. More specifically, $\frac{\pi}{4} < \theta < \frac{3\pi}{4}$ and $\frac{\pi}{4} < \phi < \frac{7\pi}{4}$, which corresponds to $45° < \theta < 135°$ and $45° < \phi < 315°$ (θ refers to the co-latitude and ϕ to the longitude). The other component of the grid is the Yang grid, which is identical to the complementary Yin grid and perpendicular to it. More specifically, the north pole of the Yang grid is located at 90 degrees longitude and 90 degrees latitude. While both grids do not have polar regions, the two combined grids cover the entire sphere. The spherical grids are defined close enough to the equatorial regions so that the finite-difference grid is almost equidistant. This allows the use of a larger iteration step. The price one has to pay is that the boundaries of each grid should be updated to capture the evolution of the field that happens within the other grid. This should be done while the optimization algorithm is running, thus increasing the

algorithm complexity. The corresponding coordinate transformation equations between the two grids are given by

$$r^e = r^n, \tag{2.8}$$

$$\sin\theta^e \cos\phi^e = -\sin\theta^n \cos\phi^n, \tag{2.9}$$

$$\sin\theta^e \sin\phi^e = \cos\theta^n, \tag{2.10}$$

$$\cos\theta^e = \sin\theta^n \sin\phi^n, \tag{2.11}$$

where the index e is used to refer to the Yin grid and the index n to the Yang grid. As the two-component grids are completely symmetrical to each other, the same expression is used to transform coordinates from the Yang to the Yin grid. The symmetry of the two grids is very convenient for the implementation of the code, because all mathematical and algorithmic procedures can operate on both grids.

2.1.3 Yin–Yang implementation

There are two basic differences between the previous version of the optimization code and the newly developed one. All numerical operations called to operate on one grid are also called to operate on the other. The lateral boundaries of each grid (which have been fixed to a potential field in previous code versions) are now updated with values taken from the complementary grid. In this way, the new method overcomes the problem of earlier codes where the lateral boundaries were required to be specified. The Yin–Yang implementation requires only boundary conditions at the photosphere and on the outer boundary. In order to update the boundaries of one grid using the values from the other, we apply the following procedure:

1. For an arbitrary grid point, we perform a coordinate transformation to find its coordinates with respect to the other grid.

2. Compute the magnetic-field vector at this point, by applying an interpolation method. It is important to note here that the new coordinates of our arbitrary point do not have to match with the coordinates of a grid point of the other grid and this is why we have to interpolate to estimate the components of the magnetic-field vector.

3. Transform the magnetic vector back to the initial grid.

Because of the symmetry of the grids, this process is identical regardless of which is the first and which is the second grid. We describe below all the steps needed for the new Yin–Yang optimization code.

1. Initialize the Yin grid by performing a potential extrapolation using the line of sight magnetogram as a boundary condition.

2. Replace the bottom boundary of the Yin grid with a vector magnetogram. Here, a synthetic one deduced from the Low and Lou solution (a semi-analytical force-free equilibrium found by Low and Lou (1990)) is used.

3. Initialize the Yang grid by coordinate transformation, interpolation, and vector transformation.

4. Calculate L with Equation 2.3 separately on both grids.

5. Add $L = L_{\text{Yin}} + L_{\text{Yang}}$.

6. The iterative Equation 2.4 is used to iterate the field towards minimizing L separately on both grids.

7. The boundaries of each grid are updated using the values of the field on the other grid (by coordinate transformation, interpolation, and vector transformation).

8. The code is terminated when L becomes stationary.

9. The final solution can be transformed to both grids.

2.2   Validation of the code

2.2.1   Method

In this section, we want to evaluate the performance of our newly developed code. The aim is to find out whether our code is able to minimize the functional L down to the numerical precision and to compare the output of our code with a known nonlinear force-free field reference equilibrium. Checking the force-freeness and comparing with a reference solution are standard procedures to validate NLFFF codes implemented on Cartesian and spherical grids. A frequently used reference solution for this aim is a semi-analytical nonlinear force-free equilibrium solution found by Low and Lou (1990). This method solves a Grad–Shafranov equation in spherical coordinates, which is invariant in the ϕ-direction, but displacements of the origin and rotation allow us to compute equilibria which change in all three spatial coordinates. It can be used to evaluate nonlinear force-free codes in 3D (as done for Cartesian geometry by, e.g., Wiegelmann 2004, Amari et al. 2006, Schrijver et al. 2006, Inhester and Wiegelmann 2006, Valori et al. 2007) and to evaluate spherical NLFFF codes (Wiegelmann 2007, Song et al. 2007, Tadesse et al. 2009, Jiang et al. 2012, Guo et al. 2012, Contopoulos 2013, Amari et al. 2013). Following these works, we use a spherical Low and Lou solution as reference to evaluate our code, which we do as follows.

1. Calculate the spherical Low and Lou solution in 3D which from now on we will call the reference solution. A field-line plot for this reference solution is shown in Figure 2.1, left panel. The reference solution was computed on a spherical grid with $n_r = 45, n_\theta = 90$, and $n_\phi = 180$ where n_r is the number of points in the radial direction, n_θ is the number of points in latitude, and n_ϕ is the number of points in longitude.

2. By using the radial component of the Low and Lou solution as a synthetic magnetogram, we performed a potential-field extrapolation on the same spherical grid, which is shown in Figure 2.1, middle panel.

3. We use the potential field as computed in the last step as initial equilibrium and the bottom boundary from the reference solution is taken as a synthetic vector map
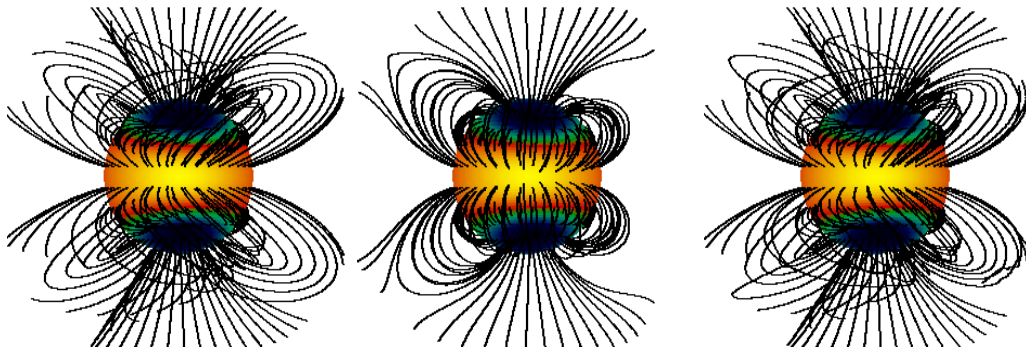
Figure 2.1: A comparison of some magnetic-field lines. The *left* panel shows the Low and Lou reference solution, the *center* panel the initial PFSS field, and the *right* panel the output from our code.

used as a boundary condition for our new code. The top boundary was selected to be either the top boundary of the potential field or the top boundary from the reference field. The effect of using these different top boundary conditions will be examined in Section 2.2.2.

4. We run the optimization code and compare the results with the reference Low and Lou solution and evaluate the influence of several effects as stated below. A visual representation of one of our outputs (dubbed Case 3, see also Table 2.1) is shown in Figure 2.1, right panel.

2.2.2   Code specifications and free parameters

A number of different parameters are used in order to control the flow of the code and to specify different conditions, as explained below. How these specifications influence the quality and computing time of our code are presented in Table 2.1.

1. Interpolation method: Specifies the order of the interpolation method used during the vector transformation process. As a first test, we use a bi-linear interpolation. Please note that the r is always identical on both grids and interpolation is needed only for the lateral directions. In principle, higher-order interpolation methods could be used.

2. Non-interpolation steps (NIS): Defines the number of optimization steps between updating the boundaries of the one grid with vectors interpolated and transformed from the other grid.

3. The initial iteration step is $\mu = 10^{-4}$, which is sufficiently small to ensure a strictly decreasing functional L if μ is kept constant.

4. Iteration-step reducer: This parameter divides μ if the functional L does not decrease after one iteration step. This is considered as a non-successful iteration step, which is refused and repeated with the reduced iteration step when running the code with a dynamically controlled time step.

5. Iteration step increaser: This parameter multiplies μ by 1.01 after every successful iteration step. This doubles the iteration step after 70 successful iterations. The optimization ensures a continuous decrease of L (see Wheatland et al. 2000). In a numerical implementation, L can increase if the iteration time-step is too large. The time-step increaser and reducer help to search for the optimum time-step, as high as possible (for a short computing time) and as low as necessary (to ensure a strictly monotonically decreasing L). The code is terminated either when the maximum number of iterations is reached or when μ becomes smaller than a threshold number: 10^{-9}.

6. The original Yin–Yang grid spans in the range $45 \leq \theta \leq 135$ and $45 \leq \phi \leq 315$. In most cases we use this standard grid, but we investigate also the effect of different (non-standard) grids.

2.2.3 Qualitative evaluation

Our first tool to validate our new code is the comparison between the field lines of the solution resulting from our code with the field lines of the reference solution and the potential solution as shown in Figure 2.1. It is evident from the reference solution in the left panel that the output of our code depicts a very good qualitative agreement of the corresponding magnetic-field lines. The potential-field model, which was used as the initial equilibrium for our code, shows large deviations in the field-line plots.

2.2.4 Quantitative evaluation

Visualizing our solution and comparing the corresponding magnetic field line plots with the reference solution as done in Figure 2.1 is a fast way to qualitatively evaluate our results. Here we use a number of quantitative criteria. The value of the functional L (Equation 2.3) after the optimization evaluates how close the resulting field is to a force-free and divergence-free state. We compute this also separately for the Lorentz-force part, defined as

$$L_1 = \int_V \left[B^{-2} \, |(\nabla \times \vec{B}) \times \vec{B}^2| \right] r^2 \, \sin\theta \, \mathrm{d}r \, \mathrm{d}\theta \, \mathrm{d}\phi, \tag{2.12}$$

and the divergence integral defined as

$$L_2 = \int_V |\nabla \cdot \vec{B}|^2 \, r^2 \, \sin\theta \, \mathrm{d}r \, \mathrm{d}\theta \, \mathrm{d}\phi. \tag{2.13}$$

Additionally, we compare our results quantitatively with the reference resolution by a number of quantitative measures, (as introduced by Schrijver et al. 2006).

Namely we use the Vector Correlation, which is defined as

$$\mathrm{VC} = \sum_i \vec{B}_i \cdot \vec{b}_i \Big/ \left(\sum_i |\vec{B}_i|^2 \sum_i |\vec{b}_i|^2 \right)^{1/2}, \tag{2.14}$$

and the Energy Percentage defined as

$$\mathrm{EP} = \frac{\sum_i |\vec{b}_i|^2}{\sum_i |\vec{B}_i|^2}. \tag{2.15}$$

The magnetic-field output from our code [$\vec{b_i}$] is compared to a reference solution [$\vec{B_i}$] (here the Low and Lou solution). For a perfect agreement of our solutions with the reference, both quantities should be unity. In order to compute these numerical quantities, the sums are taken over all N data points of the computational grid. More specifically, for the computation of each quantity, we calculate the Yin and the Yang part separately and then add them. In order to not include the overlapping region twice in the computations for these regions we use the points of the Yin grid. The vector correlation VC is an important indicator of how well the two vector fields agree, because it involves the dot products between the vectors as well as their magnitudes. The percentage of the magnetic energy EP not only helps us to compare the two vector fields but also has a physical meaning. If the energy in our solution is not close to the energy of the reference solution our model is not that useful because being able to calculate the free magnetic energy stored in the corona is one of the reasons why nonlinear force-free extrapolations are useful. Having the energy percentage close to unity tells us that overall the vectors of our vector field have the correct magnitude.

2.2.5   Comparison of different test cases

Case 0:   In this case the initial potential field and the discretization error (L, $L1$, and $L2$) are computed. This does not require optimization, but only one iteration to compute the functional L. A comparison with the reference solution is done as well. All comparison criteria should be close to their ideal values so that the potential-field solution is meaningful.

Case 1:   This case estimates the discretization error of the reference solution computed on the numerical grids. Again, no iteration was done, just one evaluation of L was computed.

Cases 2 – 4:   These are the first real tests, which use an initial potential field and both the bottom and top boundaries are prescribed from the reference solution. This ensures fully consistent boundary conditions. This set-up of boundary conditions for the Yin–Yang code is equivalent to prescribing all six boundaries of the computational box of a Cartesian NLFFF code. All quantities show an almost perfect agreement with the reference solution (Case 1). The values of L, $L1$, and $L2$ are even a bit smaller than the discretization error of the semi-analytical reference field. The reason for this is that the code optimizes these quantities on the numerical grids. The results are not affected if the update of the boundaries between the Yin–Yang grid is done after every iteration step (Case 2) or only after every 10 or 100 iteration steps as in Cases 3 and 4, respectively. When examining the convergence of the code, it seems that in Case 2 it converges faster than in Case 3 and in Case 3 it converges faster than in Case 4. This can be understood as a more frequent update of the boundaries that insures faster flow of information between the grids. When we talk about convergence speed we refer to the number of iterations needed to reduce L. The difference in convergence speed is so small that it is not visible in Figure 2.3. A significant difference is observed in the computational time, which is reduced by about 8% as the updating of the boundaries is a lot less frequent in these cases. The reduction of the execution time is not that significant when going from 10 to 100

Case	NIS	Bound	μ control	Iterations	Time	L	L1	L2	VC	EP
		Cases 1 – 7 with constant iteration time step μ								
		Yin & Yang grid with $45 \leq \theta \leq 135$ and $45 \leq \phi \leq 315$								
0	1	p	-	1	< 1	0.001	0.001	0.000	0.820	0.780
1	1	1	-	1	< 1	0.035	0.017	0.018	1.000	1.000
2	1	1	-	40 000	207	0.020	0.015	0.005	1.000	1.002
3	10	1	-	40 000	191	0.020	0.015	0.006	1.000	1.002
4	100	1	-	40 000	186	0.021	0.016	0.006	0.999	1.001
5	1	p	-	31 880	165	0.086	0.058	0.028	0.995	0.967
6	10	p	-	31 480	163	0.086	0.058	0.028	0.994	0.967
7	100	p	-	35 200	183	0.086	0.057	0.028	0.995	0.967
		Cases 8 – 13 with dynamical controlled iteration time step μ								
		Yin & Yang grid with $45 \leq \theta \leq 135$ and $45 \leq \phi \leq 315$								
8	1	1	2.0	11 407	64	0.056	0.038	0.018	0.996	0.981
9	1	1	1.5	11 744	64	0.056	0.038	0.018	0.997	0.980
10	1	1	1.25	4287	24	0.086	0.058	0.028	0.994	0.969
11	1	p	2.0	6817	37	0.102	0.074	0.028	0.992	0.951
12	1	p	1.5	7477	41	0.103	0.075	0.028	0.992	0.950
13	1	p	1.25	6922	38	0.102	0.074	0.028	0.992	0.951
		Case 14 with Yin & Yang grid with $50 \leq \theta \leq 130$ and $35 \leq \phi \leq 325$								
14	1	1	2	3357	17	1.290	1.032	0.258	0.983	0.924
		Case 15 with Yin & Yang grid with $35 \leq \theta \leq 145$ and $55 \leq \phi \leq 305$								
15	1	1	2	3055	16	1.289	1.031	0.258	0.983	0.922

Table 2.1: The specifications of our test cases (columns $1 - 4$) and a quantitative evaluation of the results (columns $5 - 11$). The first column "Case" names the test cases. The second column "NIS" the Non-Interpolation-Steps. This means the number of iterations are done on the Yin and Yang separately without communication between the two grids. Column three 'Bound' specifies the used boundary condition. Here "l" means that the Low and Lou reference field was specified in the photosphere and on the outer boundary and "p" means that a potential field was specified on the outer boundary. Column 4 "μ control"" specifies whether a constant iteration time step was used (value 1) or if and how the time-step was controlled dynamically (see the text for details). Column 5 "Iterations" shows the number of iteration steps until convergence and column 6 "Time", the computational time in minutes on Macbook pro with M1 processor. Columns $7 - 9$ "L", "L1", "L2" show the final value of the minimized functional L (see Equation 2.3) and its two parts which are the residual Lorentz force (see Equation 2.12) and the residual magnetic field divergence (see Equation 2.13). Finally, we compare the output of our code with the reference solution by the vector correlation (see equation 2.14) in column 10 "VC" and the energy percentage (see equation(2.15)) in column 11 named "EP".

non-interpolation steps as the percentage of the execution time that the code spends on doing the updates is a lot smaller in Case 3 than in Case 2. In all cases, a fixed (small) iteration time-step was used and the code was running until the maximum

number of allowed steps (40 000) was reached. The evolution of L (a decrease of almost four orders of magnitude) during the iterations is shown in Figure 2.2 and the development of the vector correlation and energy percentage in Figure 2.3. These two quantities naturally start with the potential-field values and reach almost unity at the end of the iteration.

Cases 5–7:   They are similar to Cases $2-4$ with the only difference that the bottom boundary of our computational domain was prescribed by the reference solution. The outer boundary was taken from the initial potential-field solution. These two boundaries are not necessarily consistent with each other. However, these test cases mimic the situation when the code is applied to measurements. When a full-Sun extrapolation is attempted, only photospheric magnetic-field measurements are available at present and the outer boundary is a priori unknown. This set-up of boundary conditions is comparable to specifying only the bottom boundary of a Cartesian code. The inconsistent top and bottom boundary result in slightly L, $L1$, and $L2$, a still almost perfect vector correlation, and an error of about 3% in the magnetic energy. Again the number of non-interpolation steps hardly influenced the result. Updating the interpolation only every ten steps resulted in the lowest computing time, but not by a large margin. In order to understand this difference is important to mention here that in Case 6 fewer iterations were needed to reach the state with a minimum L compared to Case 7. This is expected as the more frequent update of the boundaries ensures faster communication between the grids, thus accelerating t he convergence. On the other hand, the code runs faster when the updates are not that frequent. Therefore, the combination of these two competing procedures gives us this complex dynamics.

Cases $8-10$:   Here, instead of using a fixed, small iteration step, we controlled the iteration step dynamically. If both bottom and top boundaries are prescribed, we get a slight increase in the residual errors L, $L1$, and $L2$ compared to the cases where a fixed time step is used and an error in the energy percentage of $2-3\%$. The vector correlation is almost one. Compared with a fixed time step, we obtain a drastically reduced computational time by a factor of about 3.3 in the worst case. It is interesting to state here that while the code needs 11 000 iterations in case 8 to reach the minimum L, during the last 6000 iterations it is converging so slowly that L is reduced only 10%.

Cases $11-13$:   Here. we explore the dynamic time step control for the realistic case in which only the photospheric magnetic field is provided. The effects of potential inconsistent bottom and outer boundaries and the effects of the dynamic control of time step cumulate in a slightly higher residual error in $L1$, but not in $L2$. Compared with the fixed-time-step computation, the error in the energy percentage increases by another 3% and the magnetic energy is underestimated by 5% compared to the reference solution. The computing time decreases by a factor of about 4.5 compared to the cases with a fixed time step.

Cases 14 and 15:   Here, we investigate the effect of a non-standard Yin–Yang grid and changed the areas where both grids overlap. This was done for a case with a dynamically con-

trolled time step and the top boundary taken from the reference solution. All quantities (residual L, $L1$, and $L2$ and comparison matrices VC and EP) are worse than with the standard Yin–Yang grid, and consequently, we do not investigate further non-standard grids.
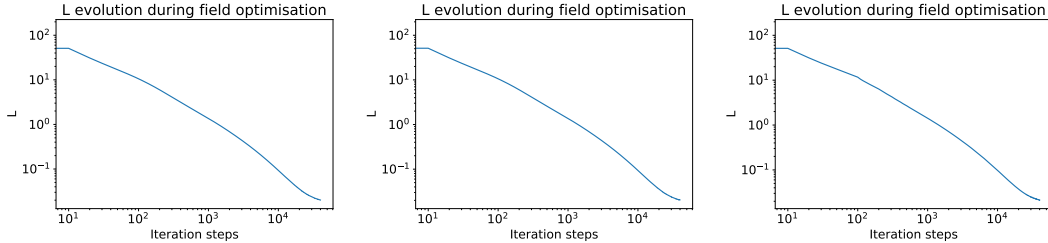

Figure 2.2: Minimization of functional L: from *left* to *right*, Cases 2, 3, and 4.
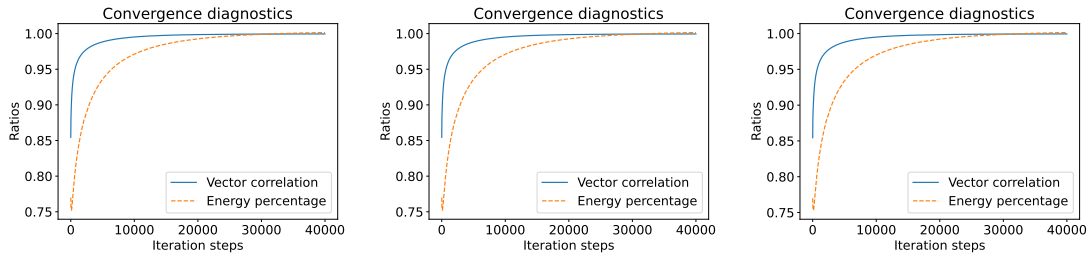

Figure 2.3: Evolution of the vector correlation and normalized magnetic energy: from *left* to *right* Cases 2, 3, and 4.

2.3   Conclusion

We developed a new nonlinear force-free optimization code implemented on a Yin–Yang grid. The quality of the solutions is comparable to the ones produced by a previous version of the spherical NLFFF code as described by Wiegelmann (2007). Please note that the previous code version did not include proper treatment of the polar regions and the earlier tests were done on a lower resolution grid. Within this work, we investigated the influence of several code specifications. The first more technical test was to investigate the new code under the condition of complete and consistent boundary conditions, where the reference solution was specified on all boundaries, which showed an almost perfect agreement of the computed equilibria with the reference solution.

Please note that the Yin–Yang grids have no lateral boundaries and only bottom and top boundaries needed to be prescribed. On the Sun, we have, however, only magnetic-field measurements in the photosphere and the top boundary conditions are unknown. A natural guess is using a potential-field source surface model to prescribe the boundary conditions on the source surface. Our code still provides a good agreement with the reference solution. The vector correlation with the reference solution has an error of

about 0.5% and the error in the magnetic energy is in the range of 3% (for a fixed small time step), and 5% (for a dynamically controlled time step). A dynamic time step does, however, reduce the computing time by about a factor of 4.5.

We also investigated to what extent the final result is influenced by how often the Yin grid and Yang grid communicate with each other (after every iteration step, after 10, and after 100 steps). It was found that these hardly influence the solution. The lowest computing time was reached if the interpolation between the two grids was done every tenth iteration step. However much tempting is to suggest using a dynamically controlled time step and grid communication at every tenth step as standard for future application to data, the combination of these parameters may have different results when working with observational data thus using an update every step is the safest suggestion. If computing time does not matter, a small, fixed time step gives somewhat more accurate results.

3 Using observed synoptic magnetograms as boundary conditions during solar minimum and maximum

3.1 Observational data

Following the validation of our newly developed force-free extrapolation code, as demonstrated through the comparison with the semi-analytical Low and Lou solution detailed in Chapter 2, we are now suitably prepared to assess its performance using a data set that more accurately reflects real-world conditions.This phase of testing will allow us to gauge the code's convergence properties and to calibrate the coronal magnetic field reconstruction when observed photospheric magnetic fields are applied as boundary conditions for the lower boundary. The temperature in the photosphere is about 5000 K and from 1 to 3 MK in the corona. In this study, we used observations taken in the time period of two Carrington rotations (CRs), namely CR2222 which covers the time period from 2019 September 19 03:43 UT to 2019 October 16 10:29 UT and CR2133 from 2013 January 25 19:57 UT to 2013 February 22 04:07 UT. We use imaging data from the Atmospheric Imaging Assembly (AIA, Lemen et al. 2012) on board the Solar Dynamics Observatory (SDO, Pesnell et al. 2012) taken in the 193 Å channel (log $T(K)$ ~6.2, hereafter AIA 193), 171 Å,(log $T(K)$ ~ 5.85, hereafter AIA 171), and 211 Å (log $T(K)$ ~6.3, hereafter AIA 211). These three images sample emission from spectral lines with formation temperatures from 0.9 to 2 MK. These AIA channels have also some contribution from transition region emission (for more details see Mou et al. 2018, and references therein). The AIA data have $0.6'' \times 0.6''$ pixel size. The three channels are combined to create multi-channel images that reveal clearly the coronal holes, that are used to match with the open magnetic field lines derived from the extrapolation models.

We also employ data from the Helioseismic Magnetic Imager (HMI, Scherrer et al. 2012). These are vector magnetograms that were converted into Carrington maps. as it is described in Liu et al. (2017). These vector synoptic maps are created by combining 20 different disk center vector magnetograms. The vector field is calculated using the Stokes parameters (I, Q, U, V) by utilizing a Milne-Eddington based inversion algorithm as it is described in Borrero et al. (2011) and Centeno et al. (2014). The 180 degree ambiguity for the transverse component of the magnetic field is treated with different methods depending on the field strength within a particular pixel and the pixel's location
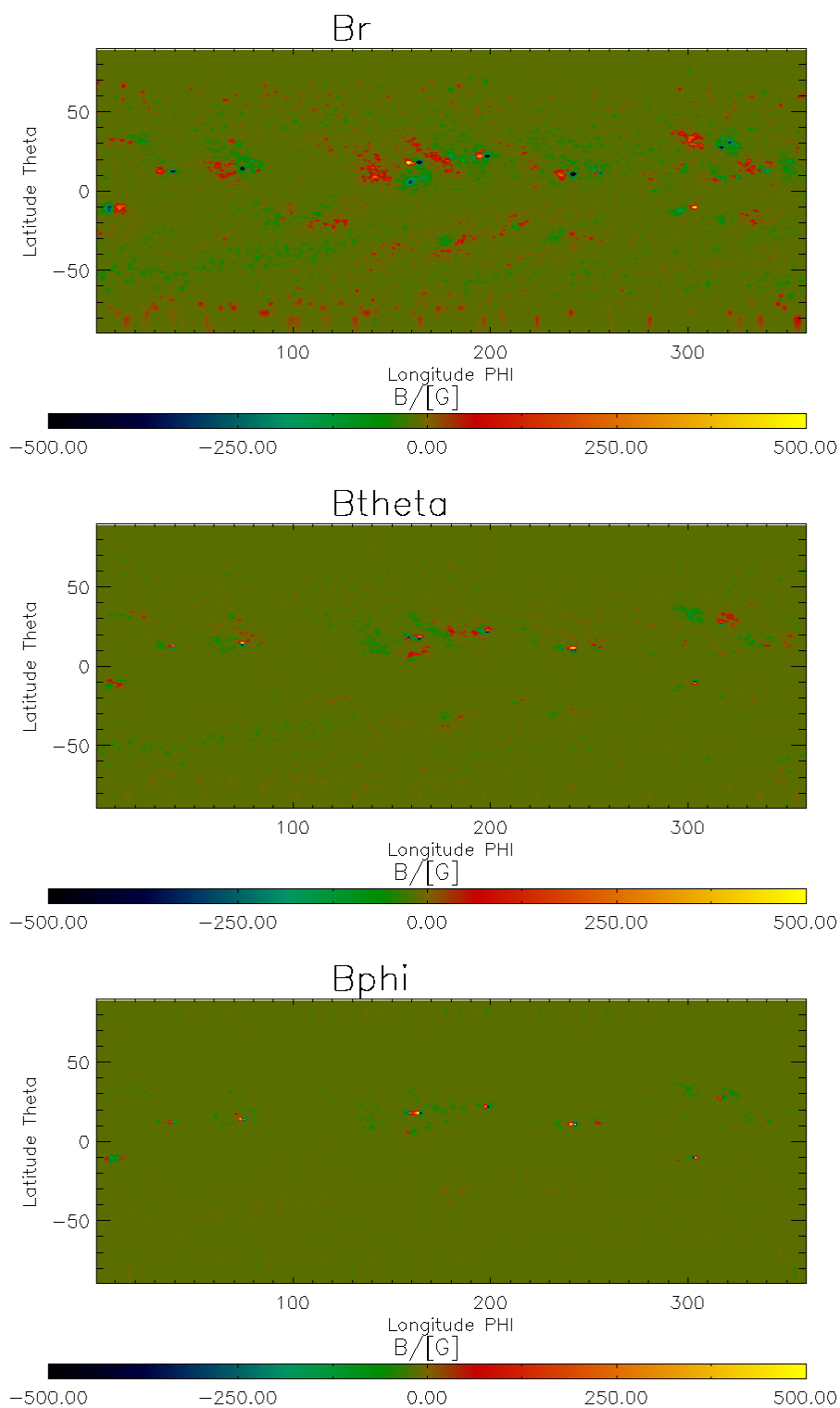
Figure 3.1: This is the synoptic vector magnetogram for CR2133 during solar activity maximum. It was observed 2013 between January 25 and February 22.

(inside or outside of an active region.) More specifically, if a pixel is located in an active region or if the strength of the transverse field is higher than 150 G then the minimum
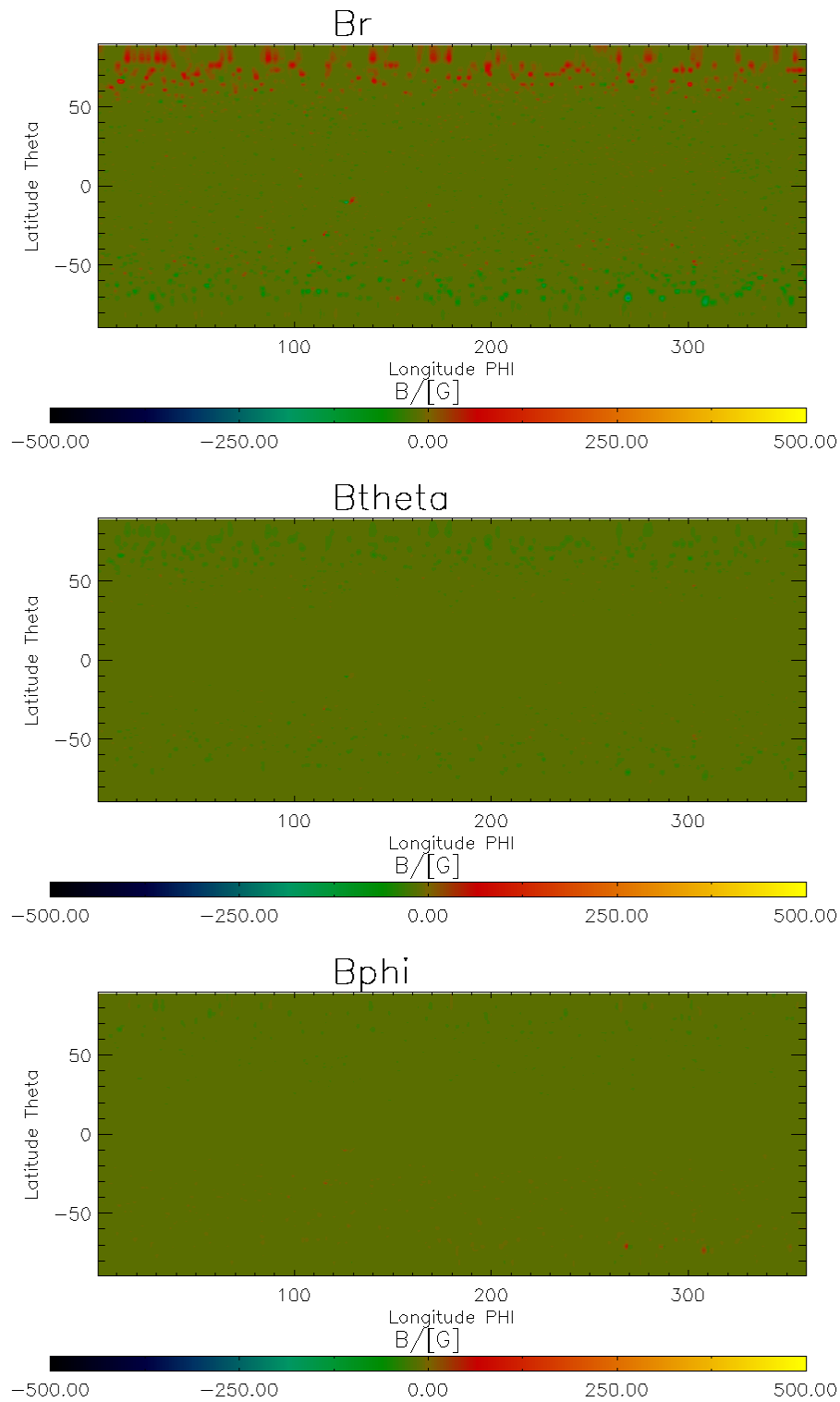
Figure 3.2: Synoptic vector magnetogram for CR2222 during solar activity minimum. It was observed 2019 between September 19 and October 16.

energy algorithm is used (Metcalf 1994, Metcalf et al. 2006, Leka et al. 2009). In the case of weaker transverse fields, three different methods are tested with the one chosen for the

particular HMI data product being the Random method. This method is selected because of its superior performance and its ability to not create artificial patterns in the data.

Figure 3.1 presents the synoptic vector magnetograms for CR2133, capturing the solar activity maximum. The panels, arranged from top to bottom, depict B_r, B_θ, and, B_ϕ, respectively. A number of active regions are prominently visible in the top panel. It is worth noting that the reliability of the transverse magnetic field component, as illustrated in the center and bottom panels, is confined primarily to the active regions.

Figure 3.2 presents the synoptic vector magnetogram for CR2222 during the period of solar activity minimum. To facilitate a direct comparison, we utilize the same color scale as the one employed for the synoptic map during the maximum solar activity phase. The top panel of the figure highlights the radial magnetic field component (B_r), revealing a notable abundance of strong magnetic flux concentrated in both polar regions, while no active regions are evident. Comparatively, the transverse magnetic flux throughout the entire map is considerably smaller in magnitude compared to the synoptic map captured during the peak of solar activity.

3.2   Adapted Yin-Yang code for using observational magnetograms as boundary conditions

It is important to note that during the process of reconstructing the Low and Lou solution, we employed synthetic boundary conditions derived directly from the three-dimensional Low and Lou solution. This methodology ensured that there were no errors or inconsistencies present within the boundary field. By contrast, the use of observed photospheric magnetic fields as boundary conditions in this next phase of testing introduces an element of complexity and uncertainty, as these realistic data contain inherent errors and inconsistencies. The outcomes of this phase offer valuable insights into the robustness of our extrapolation code under realistic operating conditions and its ability to accurately reproduce the magnetic field structure of the solar corona.

As outlined in 1.2.1.1, the magnetic field on the photosphere does not necessarily conform to the force-free assumption. The plasma β on the photosphere is of the order of unity, which is significantly higher than in the corona. As such, the possibility arises of an angle between the magnetic field and the electric current, inherently introducing a degree of 'non-force-freeness' into our model.

Another challenge associated with the use of observed magnetic fields as boundary conditions stems from the measurement process itself. Although the photospheric fields are more accurately measured than the fields in the chromosphere and the corona, the measurement process is far from simple. It involves dealing with noisy signals and requires the application of several underlying assumptions as was discussed in section 3.1. Therefore, despite the relative accuracy of photospheric field measurements, their use introduces an additional layer of complexity and potential sources of error into the model. This complexity underscores the importance of rigorous analysis and validation when using these measurements as boundary conditions in our force-free extrapolation code.

To address the impact of inconsistent boundaries and enable the convergence of the code to a force-free field, an additional term was incorporated into the optimization functional, denoted as L_3. This term was first introduced in Wiegelmann and Inhester (2010)

in Cartesian geometry and was adjusted specifically to be used with data from SDO/HMI
in Wiegelmann et al. (2012). The expanded functional was also implemented in spherical
geometry in Tadesse et al. (2011). The L_3 supplementary term is given by the following
equation

$$L_3 = \int_S (\vec{B}FF - \vec{B}obs) \cdot \vec{W}(\theta, \phi) \cdot (\vec{B}FF - \vec{B}obs) r^2 \sin\theta, d\theta, d\phi. \qquad (3.1)$$

In this equation, $\vec{B}FF$ symbolizes the field derived from the optimization, $\vec{B}obs$ signi-
fies the observed field, and $\vec{W}(\theta, \phi)$ is a function denoting the reliability of the data, which
depends on polar and azimuthal angles. More specifically, for our application, we used
the following formula for the weighting function. We decompose the observed magnetic
field on the photosphere into two components, the radial and the transverse component.
The radial component is perpendicular to the solar surface while the transverse compo-
nent is tangential to it. The function $w(\theta, \phi)_r$ is set to be unity because for HMI data we
trust the radial field. The transverse part of $w(\theta, \phi)_t$ is defined as the ratio of the magni-
tude of the transverse magnetic field over the magnitude of the maximum transverse field.
This definition reflects the fact that we consider the stronger fields more reliable than the
weaker ones. With the implementation of this weighting function, the weak field regions
will contribute less to the L_3 term and thus the optimization will 'focus' on preserving the
observed field that is more reliable.

Upon studying equation 3.1, it becomes apparent that when the derived field coincides
perfectly with the observed field, the value of L_3 becomes zero. Therefore, this term
essentially reflects the divergence of our field from the magnetogram. After the inclusion
of this term, the complete functional to be minimized is given by

$$L = \int_V \left[B^{-2} |(\nabla \times \vec{B}) \times \vec{B}|^2 + |\nabla \cdot \vec{B}|^2 \right] r^2 \sin\theta \, dr \, d\theta \, d\phi +$$
$$\int_S (\vec{B} - \vec{B}obs) \cdot \vec{W}(\theta, \phi) \cdot (\vec{B} - \vec{B}obs) r^2 \sin\theta, d\theta, d\phi. \qquad (3.2)$$

In practice, the functional 3.2 with the addition of the L_3 term will allow the bottom
boundary to differ from the observed magnetic field such as that the force-free condition
is fulfilled while trying to keep it as close as possible to the magnetogram.

3.2.1   Algorithm description with the L_3 term included

In Chapter 2 we discuss in detail the steps of the optimization algorithm when synthetic
boundaries are used. In this section we will present the steps of the adapted optimization
algorithm when the objective function is set to 3.2.

- Use the radial component of the observed magnetic field on the photosphere to com-
  pute the potential coronal field using the spherical harmonics expansion method.

- Fix the top boundary of the computational domain using the outer layer of the po-
  tential field as boundary condition. The potential field extrapolation extends up to
  the source surface where the magnetic field is set to be purely radial. Keeping the

potential field as the top boundary condition is justified because there are no strong currents so high in the solar corona.

- Start the optimization process to minimize the functional 3.2. The line search adaptive step optimization algorithm is terminated when the step size is reduced below a threshold value. In this case, this value is set to be 10^{-9}.

As in the case of synthetic Low and Lou boundary in any iteration of the optimization algorithm the grids 'communicate' by updating the boundaries of each grid. The steps followed are again coordinate transformation, interpolation and vector transformation.

For our extrapolations, we employed two distinct Yin-Yang grids with different special resolution. The low resolution grid was configured to comprise 45, 90, and 180 points along the radial, polar, and azimuth directions, respectively. The second, double resolution grid, consists of 90, 180, and 360 points along the radial, polar, and azimuth directions, respectively.

The specified number of grid points corresponds to each component of the Yin-Yang grid, where both the Yin and Yang components take the form of spherical grids. However, despite each component possessing the designated number of points, not all of these points are applicable to our computations. This is because each component grid's coverage is limited in both polar and azimuth directions, as discussed in Section 2. In our methodology, we employ the lower resolution grid as a preliminary stage before executing our computations on the higher resolution grid. The exact process works as detailed below.

- Compute the non-linear force-free field on the Yin-Yang grid for the low resolution grid.

- Interpolate the resulting solution of the previous step into the higher resolution grid.

- Use a double resolution synoptic HMI magnetogram as a boundary condition.

- Perform the computation of the non-linear force-free field in the higher resolution grid.

Adopting this procedure presents a key advantage - the interpolated field obtained in the second step is more congruent with the final solution computed on the higher resolution grid. This is in contrast to a potential field computed on the high-resolution grid, which could serve as an alternative solution. As a result, this procedure ensures a more seamless integration of the bottom boundary. This, in turn, aids the algorithm in swiftly and efficiently minimizing the loss function. Moreover, it reduces the likelihood of the algorithm becoming 'trapped' in a local minimum, enhancing the overall optimization process.

In Figure 3.3, the evolution of the terms of the functional L is shown. It is important to mention that in contrast to the case of validating the code with the Low and Lou solution, when using the observed magnetograms, the L_3 term is higher in the beginning but the other two terms L_1 and L_2 are low. This can be explained because in this case the bottom boundary is not substituted with the observed magnetogram in the beginning of the run. Therefore, the first two terms get low values and the third term gets high value because the bottom boundary is very different from the magnetogram. In the beginning of the
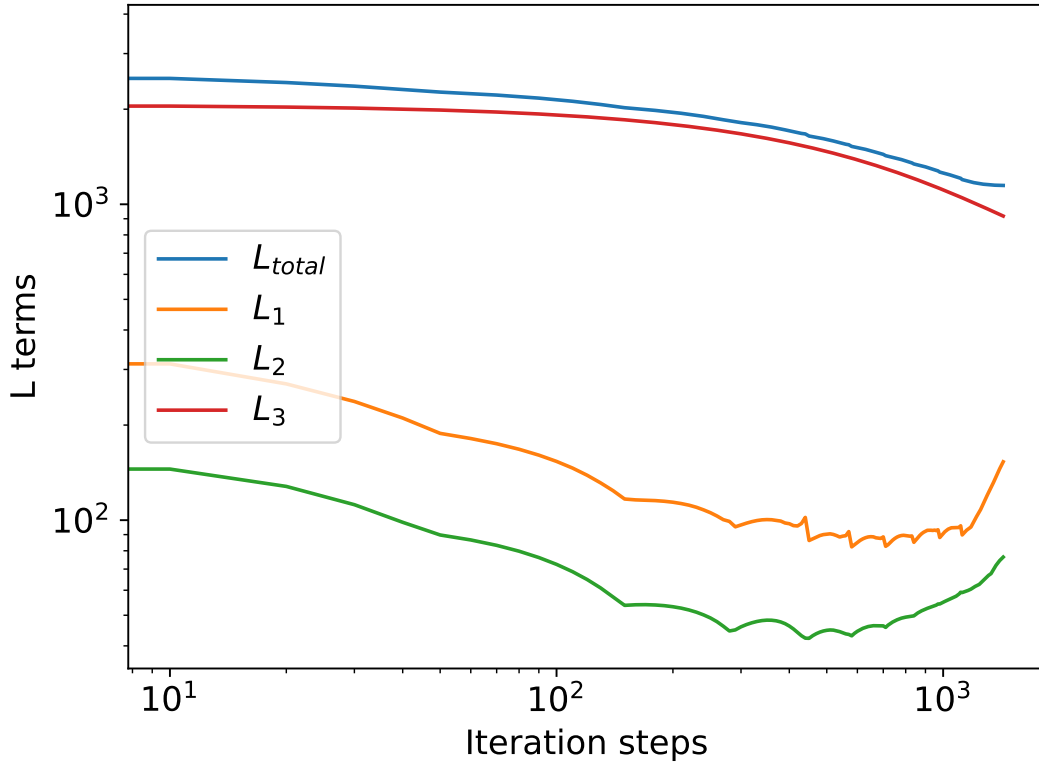
Figure 3.3: Evolution of the functional L terms during field optimization for CR2133.

optimization process the algorithm is then prioritizing the minimization of the L_3 term because is the one that has the most significant contribution to the total L. The other two terms increase but always in a way that the sum of all the terms keeps getting reduced. Figure 3.3 depicts the progression of the functional L terms. Contrary to the situation where the code is validated through the Low and Lou solution, when utilizing observed magnetograms results in an initially higher L_3 term, whereas the L_1 and L_2 terms remain low. This difference exists because in the latter case, observed magnetogram is not explicitly set as the bottom boundary at the start of the simulation but is gradually inserted to allow for a smoother convergence. As a result, the initial values for L_1 and L_2 are low, while the L_3 term is elevated due to significant diverge from the magnetogram at the bottom boundary.

During the initial stages of the optimization process, the algorithm places priority on minimizing the L_3 term, given its dominant influence on the total L value. Although L_1 and L_2 eventually increase, their collective growth is controlled such that the cumulative sum of all terms continually decreases.

3.3   Results

3.3.1   Solar activity maximum (CR2133)

In Figure 3.4 we show the projection of the synoptic map for B_r onto a solar disk image as seen 2013 February 4. Figure 3.5 shows a AIA 193 image (top left panel) and a multi-channel image (top right panel). Two large and two small equatorial plus one south pole small coronal holes are well distinguishable.
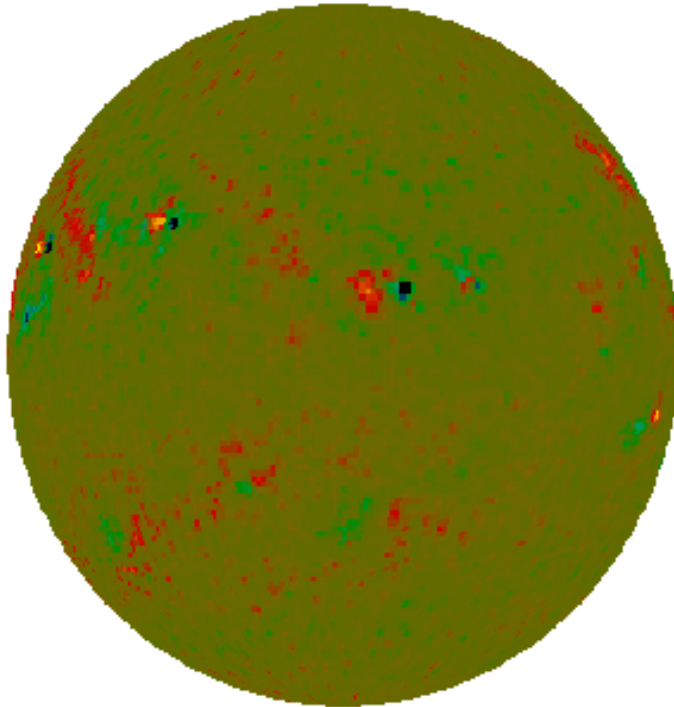

Figure 3.4: Br component of the synoptic vector map projected onto the Sun with angle of 231°. This corresponds to the Sun as seen 2013 February 4. The synoptic map has the resolution of one degree, as used as a boundary condition for the NLFFF code (360 pixel in ϕ and 180 pixel in θ for the whole sphere).

Figure 3.6, top panel, displays a selection of magnetic field lines derived from a Potential Field Source Surface (PFSS) model. This potential field was computed using a spherical harmonics expansion, as initially outlined in Schatten et al. (1969). The magnetic field lines derived from our new NLFFF Yin-Yang code are presented in the bottom panel. While there is a broad similarity in the overarching magnetic field structure between the two models, a detailed examination reveals notable discrepancies. Given that these finer details can often be challenging to discern visually, we further explore the distinctions between the PFSS and NLFFF models quantitatively. We adopted several quantitative criteria to evaluate global non-potential coronal magnetic field models as introduced in Yeates et al. (2018), and we apply these metrics in our current analysis.
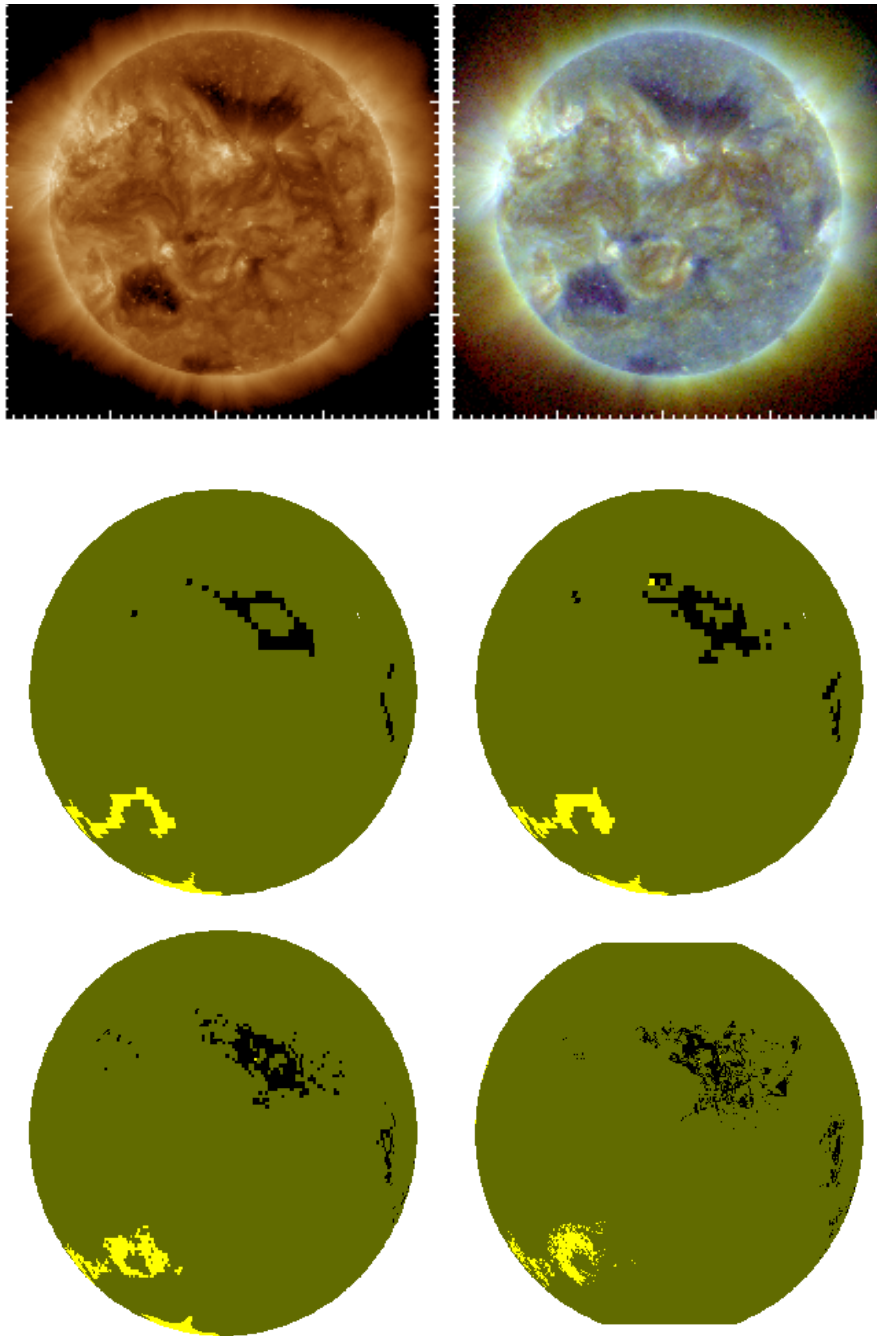
Figure 3.5: Top: EUV images (AIA 193 in the left panel and multi-channel in the right panel) as observed 2013 February 4. Equatorial coronal holes are visible in both images. Center and Bottom: The open field map from Figure 3.7 projected onto the Sun, with 231 degree at disk center to show it on February 4th 2013. Center left: potential field model, center right NLFFF with resolution of two degree. Bottom left: NLFFF with resolution of one degree. Bottom right: NLFFF with a resolution of half a degree and poles cut.

The quantities are listed in Table 3.1, where we present the result of the quantitative analysis of the selected model's influence, such as the model used (PFSS or NLFFF) and the spatial resolution (ranging from 2 to 0.5 degrees). Additionally, in the same table, we

Figure 3.6: Top: Potential field model with using spherical harmonics until l=25. Bottom: Nonlinear force-free model with a resolution of one degree. Both models are for CR2133 and shown are a few field lines as seen 2013 February 4.
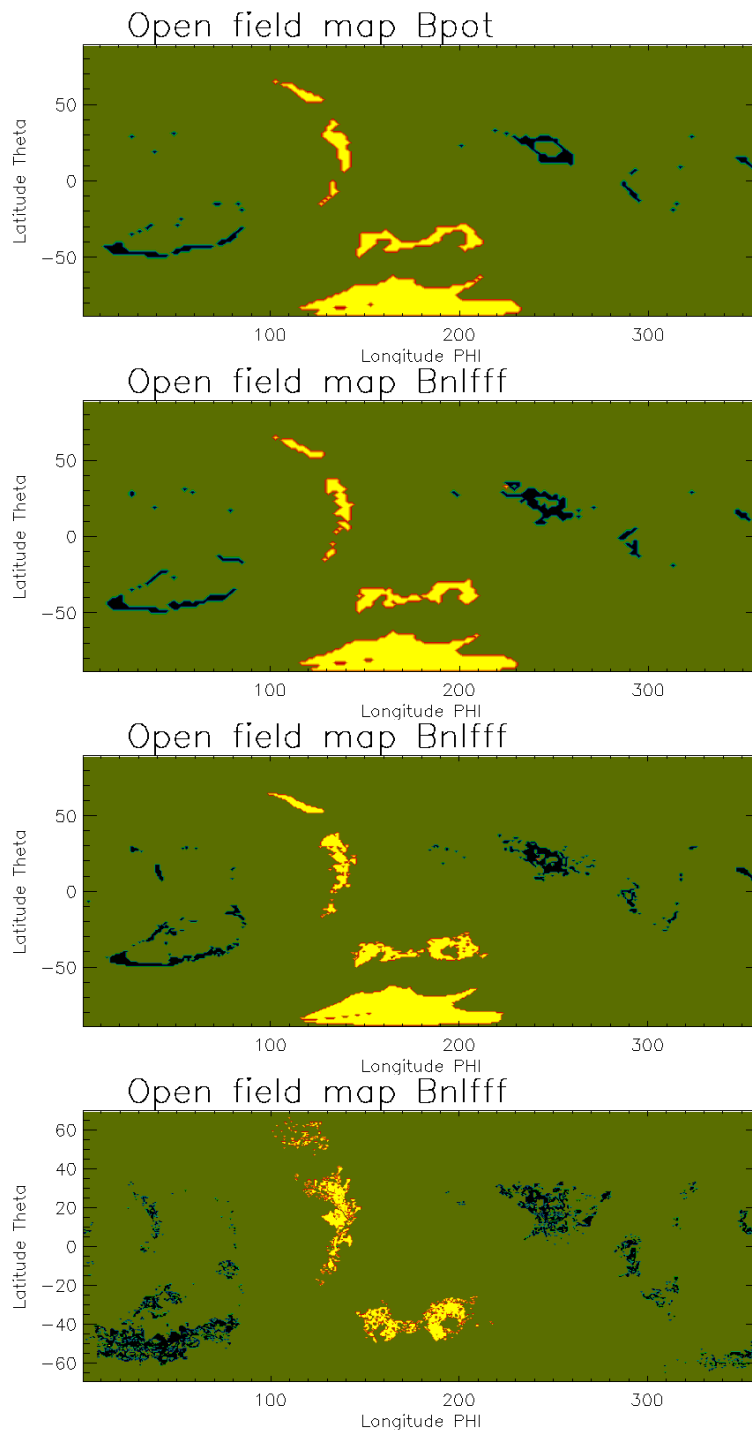
Figure 3.7: Synoptic map of the footpoints of open magnetic field lines (positive polarity in yellow and negative polarity in dark blue). From top to bottom: potential field with l until 25; NLFFF with a resolution of two degree; NLFFF with a resolution of one degree; NLFFF with high (0.5 degree) resolution, both poles are cut by 20 degree.
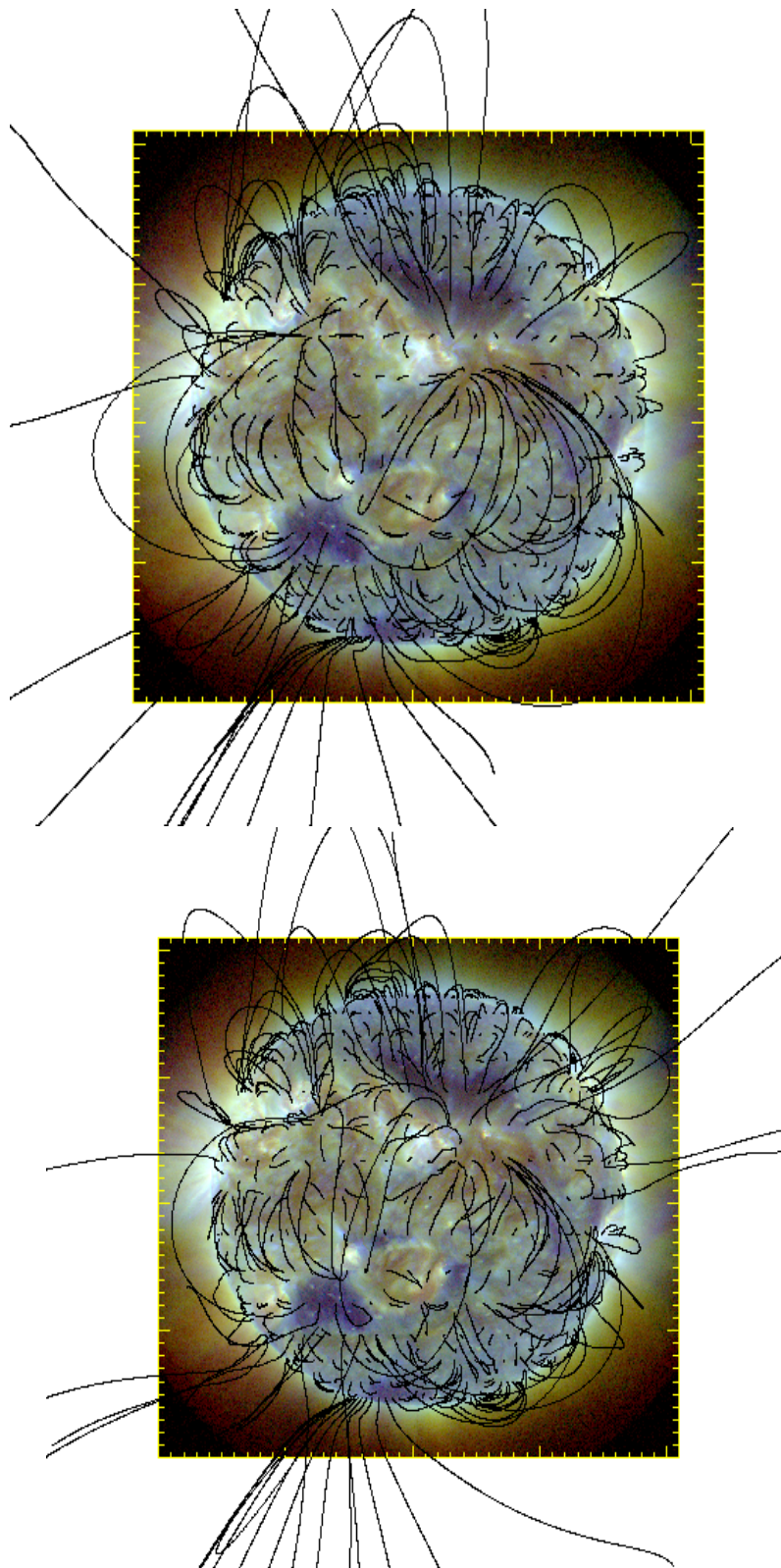
Figure 3.8: Overplotted the same magnetic-field lines as in Figure 3.6 onto a coronal multi-channel image. It is visible that the open field lines are routed in the polar regions as well as in the equatorial coronal holes. Top: Potential field model. Bottom: NLFFF model.

examine the impact of extending the computations to the solar polar regions using our new Yin-Yang code, comparing the results to those obtained from a regular finite difference spherical grid, which excludes a 20-degree range near the poles in the computational domain. We calculate the total magnetic energy and total magnetic flux, estimating these quantities for the solar surface and at distances of 1.1, 1.5, and 2.5 solar radii. The methodology employed here follows the same process as described in Yeates et al. (2018). The magnetic energy is defined through a volume integral, while the magnetic flux is defined through a surface integral. Therefore, the specified radii represent the location of the spherical surfaces for the magnetic flux computation.

Car.	Model	poles	res.	Energy	flux $r = 1.0$	flux $r = 1.1$	flux $r = 1.5$	flux $r = 2.5$
2133	PFSS	Yes	$l \leq 25$	$1.84\,10^{26}$ J	$3.13\,10^{15}$ Wb	$1.16\,10^{15}$ Wb	$4.01\,10^{14}$ Wb	$2.41\,10^{14}$ Wb
2133	NLFFF	Yes	$2.0°$	$2.87\,10^{26}$ J	$3.09\,10^{15}$ Wb	$1.23\,10^{15}$ Wb	$4.15\,10^{14}$ Wb	$2.41\,10^{14}$ Wb
2133	NLFFF	Yes	$1.0°$	$2.60\,10^{26}$ J	$3.13\,10^{15}$ Wb	$1.23\,10^{15}$ Wb	$4.00\,10^{14}$ Wb	$2.44\,10^{14}$ Wb
2133	PFSS	No	$l \leq 25$	$1.79\,10^{26}$ J	$3.08\,10^{15}$ Wb	$1.08\,10^{15}$ Wb	$3.63\,10^{14}$ Wb	$2.17\,10^{14}$ Wb
2133	NLFFF	No	$2.0°$	$2.94\,10^{26}$ J	$2.98\,10^{15}$ Wb	$1.32\,10^{15}$ Wb	$4.20\,10^{14}$ Wb	$2.19\,10^{14}$ Wb
2133	NLFFF	No	$0.5°$	$2.58\,10^{26}$ J	$3.04\,10^{15}$ Wb	$1.40\,10^{15}$ Wb	$4.30\,10^{14}$ Wb	$2.24\,10^{14}$ Wb
2222	PFSS	Yes	$l \leq 25$	$3.07\,10^{25}$ J	$8.39\,10^{14}$ Wb	$5.89\,10^{14}$ Wb	$4.58\,10^{14}$ Wb	$3.85\,10^{14}$ Wb
2222	NLFFF	YES	$2.0°$	$3.39\,10^{25}$ J	$9.96\,10^{14}$ Wb	$6.36\,10^{14}$ Wb	$4.54\,10^{14}$ Wb	$3.85\,10^{14}$ Wb
2222	PFSS	No	$l \leq 25$	$8.99\,10^{24}$ J	$5.89\,10^{14}$ Wb	$3.16\,10^{14}$ Wb	$2.20\,10^{14}$ Wb	$1.88\,10^{14}$ Wb
2222	NLFFF	No	$2.0°$	$1.83\,10^{25}$ J	$6.96\,10^{14}$ Wb	$3.84\,10^{14}$ Wb	$2.24\,10^{14}$ Wb	$1.86\,10^{14}$ Wb
2222	NLFFF	No	$0.5°$	$1.83\,10^{25}$ J	$8.81\,10^{14}$ Wb	$3.84\,10^{14}$ Wb	$2.22\,10^{14}$ Wb	$1.86\,10^{14}$ Wb

Table 3.1: Physical quantities from the different models. The first column 'CR' gives the the chosen synoptic Carrington vector-magnetogram maps ('CR', 2133 during solar activity maximum and 2222 during solar activity minimum. The second column 'Model' lists the used models, either potential field source surface model (PFSS) or nonlinear force-free field model (NLFFF). The third column 'Poles': 'Yes' means that the entire sphere including the polar regions was modelled and 'No' that 20 degree on both poles have been cut. In the fourth column 'Res' either the spatial resolution for the NLFFF modeling or the maximum number l of spherical harmonics for PFSS are given. The fifth column provides the total integrated magnetic energy J. In column 6–9 we list the magnetic flux 'Fl' at different spherical shells at $1.0, 1.1, 1.5, 2.5$ solar radii 'r', respectively.

It is evident that the energy for NLFFF is considerably higher when compared to PFSS, whereas the differences in fluxes are smaller. This could be explained by the fact that the magnetic energy is proportional to the square of the magnetic field while the magnetic flux is linearly proportional to the magnetic field. Moreover, the magnetic field becomes more and more potential with increasing height in the corona and the computed surface integrals are not affected from the field at lower heights. In the case of the volume integral, the lower parts of the solar corona are taken into account, dominate the volume integral, and thus introducing this higher difference between the potential and force-free energy. In the case of CR2133, the effects of resolution are minimal, and including or excluding the polar regions only has a moderate impact on the global magnetic field structure. This can be attributed to the fact that the majority of the magnetic flux is concentrated in the active regions, which are located closer to the equator. However, as we will observe later, this scenario is significantly different for CR2222 observed during solar activity minimum, where the flux in polar regions has a more profound impact on the global magnetic field in the solar corona.

In Figure 3.7, we present the results of investigating another significant feature: the footpoints of open magnetic field lines in the photosphere, depicted on a synoptic map. The top panel shows the results obtained from the PFSS model, while the subsequent panels showcase the NLFFF model with varying spatial resolution. The second-from-top panel displays the NLFFF model with a polar region at a resolution of 2.0 degrees, followed by the third-from-top panel representing a resolution of 1.0 degrees. The bottom panel illustrates the NLFFF model with poles cut at a resolution of 0.5 degrees. While the general location of the footpoints appears similar across all models, there are notable differences in detail. The footpoint locations derived from higher-resolution NLFFF models are slightly larger and exhibit greater complexity compared to those obtained from PFSS. In all models, the footpoints along the equator align with the positions of coronal holes observed in coronal images. Naturally, in the experiment where the poles are excluded, the large polar coronal hole in the south, which is visible in the top three panels, is not found.

Moving back to Figure 3.5, we project the synoptic open field maps onto the sun and compare them with the locations of the coronal holes. The results show that the open field lines are well rooted within the coronal holes. Finally, Figure 3.8 presents a multi-channel image with a selection of field lines overlaid on it (top for PFSS and bottom for NLFFF). This again confirms that open field lines are rooted in the coronal hole regions.

3.3.2   Solar activity minimum (CR2222)

In Figure 3.9, we project the radial component of the synoptic map onto the surface of the Sun as seen 2019 September 25. Furthermore, Figure 3.10 presents in the top left panel an AIA 193 image, along with a top right panel showcasing a multi-channel image constructed from quasi-temporal images. These images vividly display a large polar coronal hole located at the north pole, extending across a significant portion of the equatorial region.

Figure 3.11 shows in the top and bottom panel a few selected field lines for a PFSS and NLFFF model, respectively. Compared with the solar activity maximum case seen in Figure 3.6 the magnetic field structure in minimum is much less complex and the large scale structure depicts mainly a dipole. In Table 3.1 we investigate the same quantities as for the maximum case. The results are, however, very different. Here it makes a large difference if we include or exclude the polar regions. This is no surprise, however, because of the large amount of flux seen in the polar regions in the synoptic map. Consequently there is about a factor of two differences in the magnetic energy and magnetic fluxes if we include or exclude the polar regions. The magnetic energy of NLFFF is only about 10% higher compared with PFSS for the full sphere case. This is also no surprise, because free magnetic energy is mainly stored in active regions, which are absent during activity minimum.

Figure 3.12 illustrates the synoptic maps displaying the footpoints of open magnetic field lines. In the top panel, we observe the results obtained from a PFSS model, while the second panel showcases the findings from an NLFFF model that includes both polar regions. Both models successfully capture the presence of the polar coronal holes. However, for an unknown reason, the footpoints of the equatorial extension of the hole are not depicted in these panels. Interestingly, when we exclude the polar regions, as
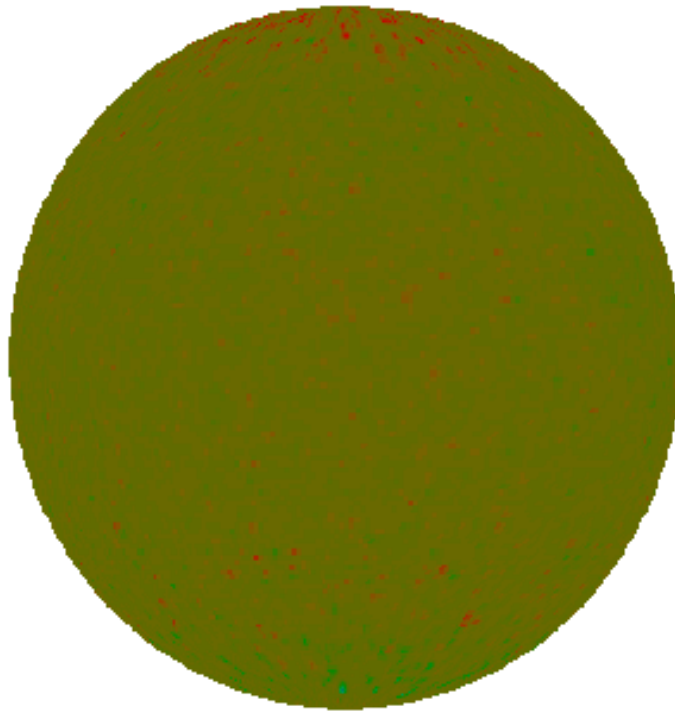
Figure 3.9: Br component of the synoptic vector map projected onto the Sun with an angle of 270°. This corresponds to the Sun as seen 2019 September 25. The synoptic has the resolution of half a degree, as used for the boundary condition of the NLFFF code (720 pixel in ϕ and 280 pixel in θ for the whole sphere, where the polar regions have been cut by 20 degrees).

demonstrated in the third panel and the bottom panel with varying spatial resolutions, the footpoints of the equatorial hole become clearly visible. We are currently unable to comprehend the underlying reasons behind this particular result and further investigation is required to gain a better understanding. The first possible reason to explain the inability of the correct description of the coronal whole when the polar regions are included is the quality of the vector field measurements at the solar poles. For line-of-sight magnetograms Gosain et al. (2013) shows that there are higher errors in higher latitudes. In Centeno et al. (2023) the authors create synthetic magnetic fields on the solar poles and then use the inversion algorithm to study how well they can retrieve the synthetic field.

The inversions undercount the pixels lacking any Line-Of-Sight (LOS) field component. They also extract more potent transverse fields than those actually present in the simulation. the count of purely transverse fields, which are those at an angle of 90 degrees is significantly misjudged. Finally, they overestimate the number of pixels where the transverse component aligns with the foreshortening direction, meaning at angles of either 0 degrees or 180 degrees. When observing the solar magnetic field at the poles from Earth, foreshortening occurs because we're viewing these regions at an oblique angle. This could lead to an overestimation of the pixels where the transverse (perpendicular
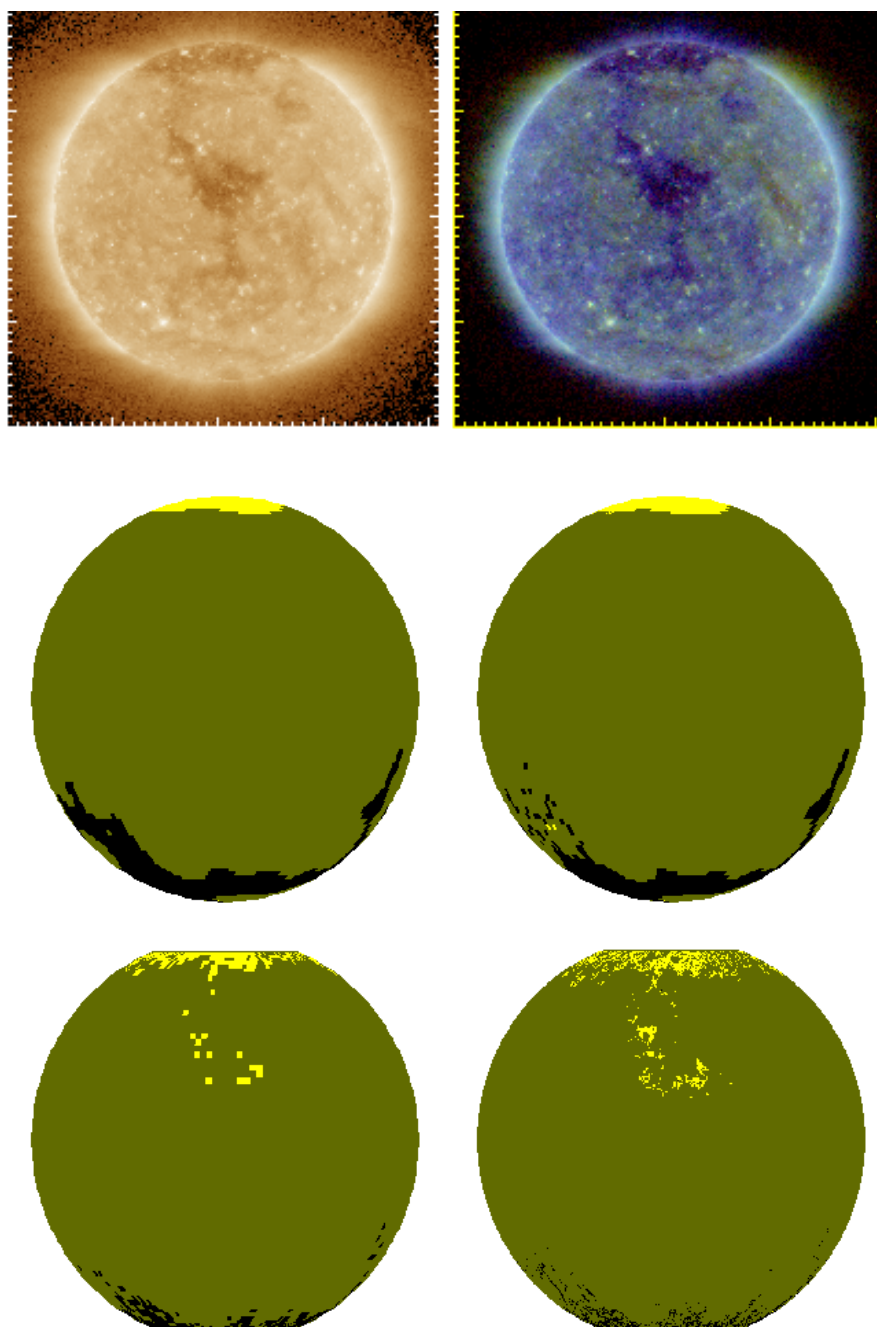
Figure 3.10: Top: Two images (left: AIA 193 and right: multi-channel) taken 2019 September 25. Middle: The open field map from Figure 3.12 projected onto the Sun, with 270 degree to show it 2019 September 25. The left map was done with a potential field model and the right with a NLFFF model and 2 degree resolution. Bottom left: a NLFFF model with poles cut and 2 degree resolution. Bottom right: NLFFF model with half degree resolution and poles cut.

to Earth-Sun line) component of the magnetic field aligns with the direction of foreshortening. In our computations we use a weighting functions/mask for the transverse component of the magnetic field that is trusting more the stronger fields. When working with
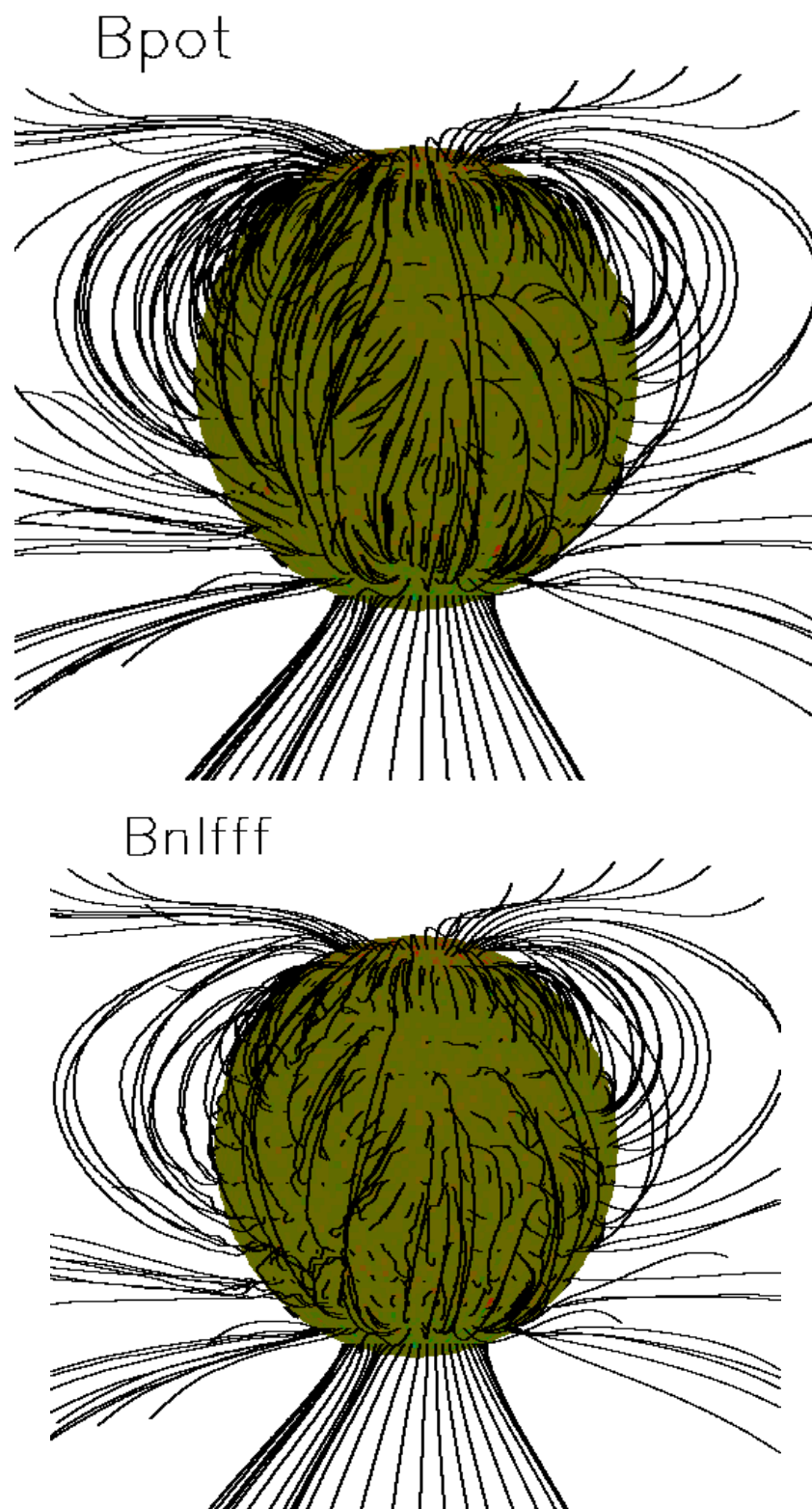
Figure 3.11: Top: Potential field model with max $l = 25$. Bottom: NLFFF model with two degree resolution. Both models are for CR2222 with overplotted the same number of field lines as seen at 2019 September 25.
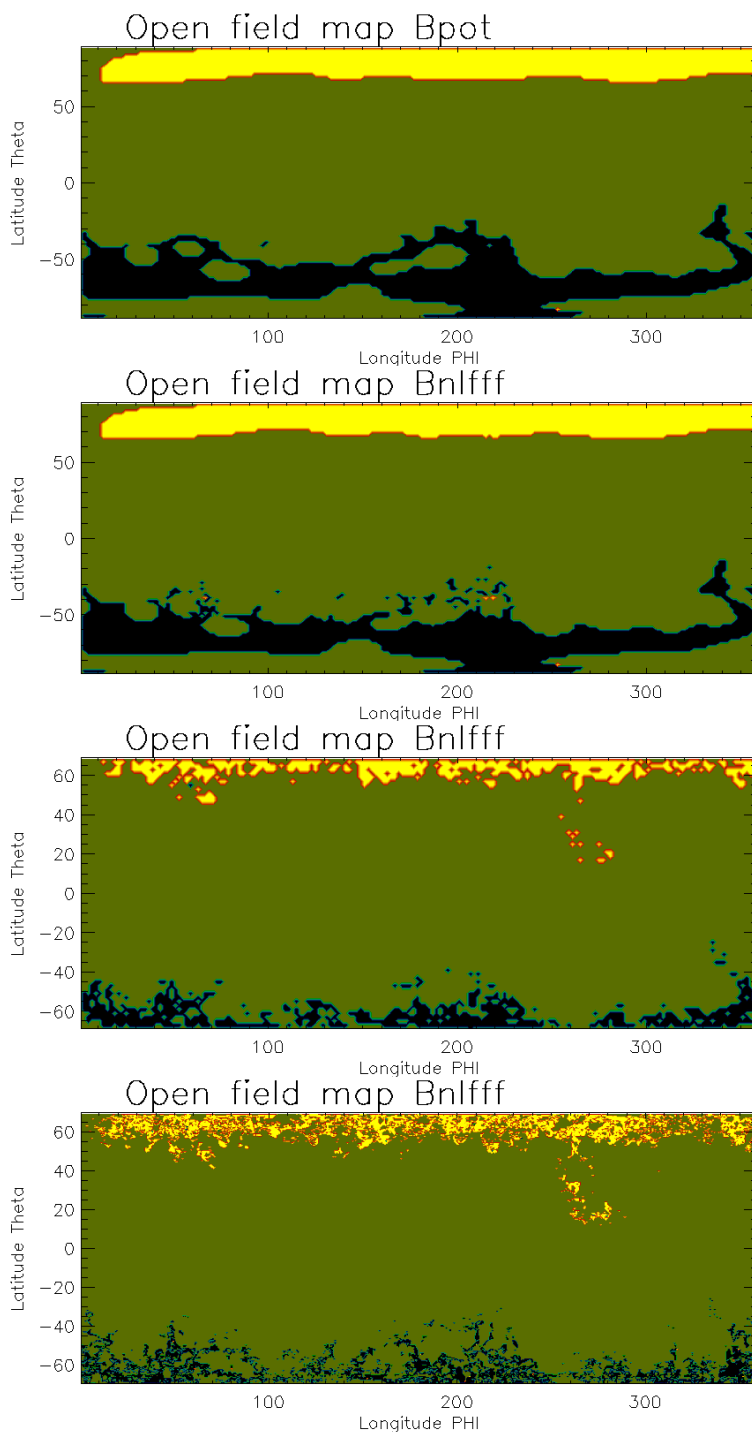
Figure 3.12: Synoptic map of the footpoints of open magnetic field lines for solar activity minimum CR2222 (positive polarity in yellow and negative polarity in dark blue). From top to bottom: Based on potential field extrapolations; Full sphere NLFFF with a 2 degree resolution; NLFFF with poles cut 2 degree resolution; Resolution of half degree and poles cut.

the regions of the sun close to the equator, the transverse field to the line-of-sight and the transverse field to the radial direction are basically the same direction. When moving away of the equator and closer to the poles these two directions start deviate the one from the other. Therefore, although this definition of the mask was suitable for the codes that did not include the polar regions their definition should probably adapted to reflect the reduced reliability of the data towards the polar regions.

Moving on to Figure 3.13, we superimpose open magnetic field lines onto a multi-channel image of the solar corona. The top panel of the figure shows results from a low-resolution NLFFF model, which includes the polar regions. This visualization reveals both polar coronal holes as well as an open field line within the equatorial coronal hole. Contrastingly, the bottom panel presents high-resolution NLFFF results, where the polar regions have been excluded. As one might expect, this model does not capture the polar holes. However, it does indicate a greater amount of open field in the vicinity of the observed equatorial hole. Our conclusion from these comparisons is that the problematic polar magnetic field data when included in the boundary conditions negatively affect the quality of the solution.

Back to Figure 3.10 (middle and bottom rows), we project the synoptic maps onto a representation of the Sun as observed 2019 September 25. The most noticeable feature from this projection is that the runs without inclusion of the polar region are capable of reconstructing an equatorial hole. There is a slight shift in the footpoints relative to the hole observed in the images, which is an aspect requiring further investigation. However, the runs that consider the full sphere do not manifest this feature.
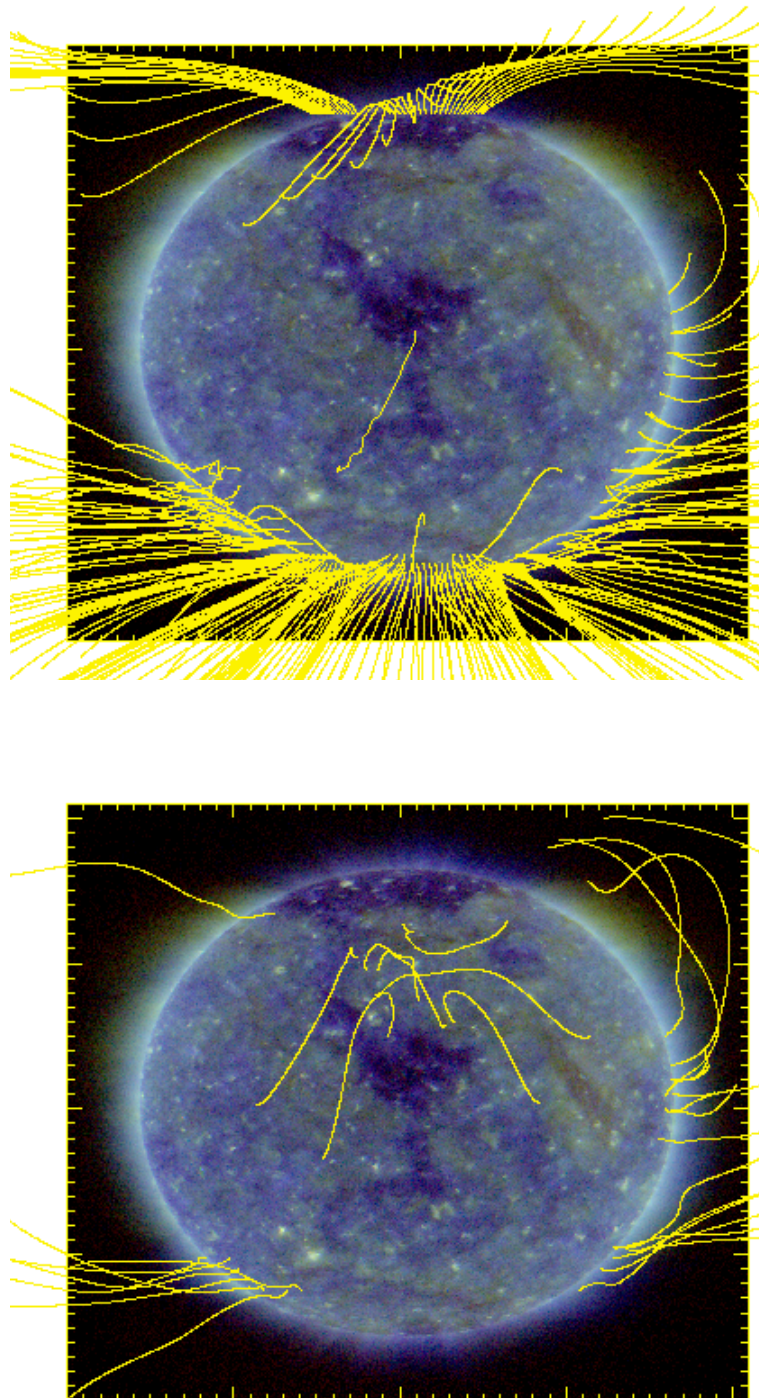
Figure 3.13: Open magnetic field lines plotted onto a multi-color EUV image. Top: a full sphere NLFFF model including the poles (resolution 2 degree) and Bottom: a NLFFF model with polar regions cut (resolution half a degree). The full NLFFF run outlines well the polar coronal holes and shows one open field line in the equatorial hole. The run with poles cut shows more field lines in equatorial regions, but does not catch the polar magnetic-field lines.

4 Conclusions

4.1 Overview

This thesis introduces a new numerical code capable of reconstructing the coronal magnetic field under the non-linear force-free approximation. A unique attribute of this code lies in its implementation on a Yin-Yang grid, which allows for the incorporation of solar poles in the calculations, a task only one other existing code can currently accomplish, see Jing et al. (2013).

Our model's validity was established by using a non-linear force-free semi-analytical solution known as 'the Low and Lou solution'. We extracted synthetic boundary conditions from this benchmark solution and then compared our reconstructed 3D magnetic field with the semi-analytical solution as outlined in detail in Chapter 2. The success of this validation provided the impetus for us to apply observed magnetograms as boundary conditions to our model, thus enabling the reconstruction of the field for a more realistic scenario.

To accomplish this, it was necessary to augment the numerical model so as to be able to manage inconsistent and noisy boundary conditions. Despite these challenges, our code exhibited exceptional performance when the generated field lines are compared to observed coronal structures.

This research represents a pioneering effort in extrapolating the solar magnetic field in the solar corona, particularly as it incorporates the polar regions within the computational domain, something prior computations of force-free fields from measured vector magnetograms did not attempt. While magnetic-field data from polar regions pose certain challenges, our study demonstrates that during solar maximum activity phase (CR2133) when the majority of the magnetic flux is concentrated outside the polar regions, the reconstructed field accurately replicates the locations of the coronal holes and coronal loops. However, during solar minimum activity (CR2222), when significant flux is located within the polar regions, the data quality has a more substantial impact on the reconstructed field, leading to a discrepancy with the observed field.

The Solar Orbiter mission (see Forveille and Shore 2020) will provide more reliable measurements for the magnetic field on the photosphere at the solar poles thereby supplying us with complimentary data for the HMI synoptic vector maps that can be used to 'fill' the polar regions.

4.2   New directions of research

The successful implementation of the non-linear force-free optimization code on a Yin-Yang grid is promising for advancements concerning not only the global modeling of the corona, but of the heliosphere as well. The focus of the current research was selected to be the force-free fields because the force-free approximation stands a complexity level above the widely used Potential Source Surface model. Our examination of large-scale structures suggests that the force-free approximation is adequate for encapsulating these features. A significant distinction between our model and the potential field model lies in the capability of the force-free scenario to calculate the magnetic free energy, a crucial physical quantity in the corona. The Potential Field Source Surface model, despite its simplicity, is widely adopted as a boundary condition for computational models of the outer corona and the heliosphere. It is even utilized in some of the most cutting-edge numerical models for space weather prediction, such as the European Heliospheric Forecasting Information Asset (EUHFORIA) (see Wang et al. 2018). However, the use of a simplistic model like the potential field source surface model can have implications on the quality of the model built upon it. This fact is highlighted in Koukras et al. (2022), which underscores the significance of the magnetic field structure when back-mapping the fast solar wind.

Our code, with its proven capability to accurately reproduce the location of open and closed field lines in the solar corona, could serve as a model for various purposes. For instance, it could be used for setting initial conditions in time-dependent models like EUHFORIA. Additionally, it could be a valuable tool in the identification and back-mapping of the solar wind. As such, our code offers a promising approach in improving the quality and accuracy of predictive space weather models.

A future iteration of this numerical model could be advanced further by incorporating not only a Yin-Yang grid but also a non-uniform grid. This modification could be particularly beneficial in modeling active regions with higher spatial resolution. The observed magnetic field in the active regions is stronger and thus the component of the magnetic field vertical to the line of sight is more reliable. Therefore, the regions with higher magnetic field can be modeled with higher spatial resolution enabling us to perform a better reconstruction of the coronal loops within the active regions. This more detailed reconstruction could also be utilized for the one-to-one comparison of the loops reconstructed by our code with the ones found in observations. In cases where more than one instruments are observing, the same active region stereoscopy could be an additional tool to extract the 3D structure of the observed loops like in Wiegelmann and Neukirch (2002) thus enabling a more rigorous comparison. On the contrary, in the quiet Sun, where the magnetic fields at the photosphere is much weaker and the signal-to-noise ratio for the vertical to the line-of-sight component is very low, a very high resolution is probably not so beneficial for using it as boundary condition for global coronal magnetic field models. Therefore, this feature of being able to select the appropriate resolution depending on the data reliability, makes the implementation of a non-uniform spatial grid a promising approach. Our code utilizes a line search gradient descent algorithm as the optimization algorithm. While this algorithm has shown success in minimizing the objective functional L, it is worth exploring other optimization algorithms, as discussed in Section 1.6. Several of these algorithms have gained popularity in the field of machine learning and

artificial intelligence for their ability to achieve faster convergence across various types of objective functions.

To enhance the efficiency of our code and further minimize the objective function within the parameter space, it would be interesting to investigate the utilization of more advanced algorithms. This avenue of research could potentially lead to discovering that one of these algorithm offers improved speed and better optimization results.

The use of boundary conditions that are the output of other numerical models is another interesting way to possibly improve our global extrapolations. There are models that simulate the magnetic field on the photosphere that extend their computations up to the solar poles. For example, the flux transport models first introduced by Leighton (1964) predict the motions of the solar magnetic fields thus being able to approximate the polar field as well (see Yeates et al. 2023, for a recent review on flux transport models). A data product that is publicly available is the ADAPT maps based on the model in Worden and Harvey (2000) and described in Arge et al. (2010). The ADAPT maps do not currently include a transverse component of the magnetic field on the photosphere, but only the radial component. Therefore, they cannot be used directly in our model. A way to overcome this difficulty would be to use the radial field extracted from the ADAPT maps only for the polar regions and the HMI vector magnetogram data for the rest of the computational domain.

Another way in which our 3D full-sphere coronal field reconstruction could be utilized is by providing more accurate boundary conditions for active region coronal magnetic field models. Because our code is using the Yin-Yang grid which effectively covers the whole volume of the spherical shell of the solar corona there is no need for additional boundary conditions at the lateral boundaries as is the case when the computations are restricted to exclude the polar regions. In the case of modeling active regions, there is the need for prescribing six surfaces both in spherical and Cartesian geometry (bottom boundary, top boundary, and four lateral boundaries). The bottom boundary is always chosen to be the observed magnetogram but for the other five boundaries, the potential field is used as it is done for example in Wheatland et al. (2000). The resulting magnetic field from our global extrapolations could be used as an alternative way to prescribe the lateral boundaries for these models. Active regions are not isolated systems but are sometimes connected with other active regions through interconnecting coronal loops as it is shown in Du et al. (2018). Therefore, prescribing the boundaries of the corona above an active region using our global coronal model could lead to a more accurate reconstruction of the active regions as well.

Our code, which leverages a line-search gradient descent algorithm to solve systems of partial differential equations, offers the distinct advantage of expandability. In essence, the objective or loss function can be broadened to encompass additional terms. This terms' minimization then aligns with the solution of further equations, augmenting the code's functionality.

For instance, in Wiegelmann et al. (2020), integrated terms pertain to plasma pressure and solar wind flow into the calculations. The stationary MHD code, however, is designed around a finite differences numerical grid, which precludes the inclusion of polar regions in the computations.

To enhance our work, we propose incorporating the objective functional form from Wiegelmann et al. (2020) into the Yin-Yang code. In doing so, it is feasible to include

additional terms describing the centrifugal and Coriolis forces, thus enriching the complexity and accuracy of our model.

This advancement is critical, especially for broadening the model's scope beyond the source surface, extending up to 10 solar radii. At this distance, the Parker Solar Probe will be capable of providing in-situ measurements that serve to validate our computational models. Therefore, integrating these forces can create a more comprehensive and precise model, positioning us well for future scientific discoveries.

Bibliography

Altschuler, M., Newkirk Jr, G., 1969a, The photospheric magnetic flux and the force-free field of the solar corona, Solar Physics, 9, 131–149

Altschuler, M. D., Newkirk Jr, G., 1969b, Magnetic fields in the solar corona: I. models and general characteristics, Solar Physics, 9, 131–149

Amari, T., Boulmezaoud, T. Z., Aly, J. J., 2006, Well posed reconstruction of the solar coronal magnetic field, A&A, 446, 691–705

Amari, T., Aly, J. J., Canou, A., Mikic, Z., 2013, Reconstruction of the solar coronal magnetic field in spherical geometry, A&A, 553, A43

Arge, C. N., Henney, C. J., Koller, J., Compeau, C. R., Young, S., MacKenzie, D., Fay, A., Harvey, J. W., 2010, Air Force Data Assimilative Photospheric Flux Transport (ADAPT) Model, in Twelfth International Solar Wind Conference, (Eds.) M. Maksimovic, K. Issautier, N. Meyer-Vernet, M. Moncuquet, F. Pantellini, vol. 1216 of American Institute of Physics Conference Series, pp. 343–346

Armijo, L., 1966, Minimization of functions having lipschitz-continuous first partial derivatives, Pacific Journal of Mathematics, 16, 1–3

Aschwanden, M. J., 2005, Physics of the Solar Corona. An Introduction with Problems and Solutions (2nd edition), Springer

Babcock, H. W., 1961, The Topology of the Sun's Magnetic Field and the 22-YEAR Cycle., ApJ, 133, 572

Birkhoff, G. D., von Neumann, J., 1946, An iterative method for the solution of linear equations, Bulletin of the American Mathematical Society, 52, 369–384

Borrero, J. M., Tomczyk, S., Kubo, M., Socas-Navarro, H., Schou, J., Couvidat, S., Bogart, R., 2011, VFISV: Very Fast Inversion of the Stokes Vector for the Helioseismic and Magnetic Imager, Sol. Phys., 273, 267–293, `0901.2702`

Bossavit, A., 2003, Delaunay triangulation and meshing: Application to finite elements, Reviews of modern physics, 75, 1201–1259

Bottou, L., 2010, Large-scale machine learning with stochastic gradient descent, in Proceedings of COMPSTAT'2010: 19th International Conference on Computational StatisticsParis France, August 22-27, 2010 Keynote, Invited and Contributed Papers, pp. 177–186, Springer

Braess, D., 2007, Finite Element Methods and Navier-Stokes Equations, Cambridge University Press

Brandt, A., 1977, Multi-level adaptive solutions to boundary-value problems, Mathematics of Computation, 31, 333–390

Brenner, S. C., Scott, L. R., 2007, The Mathematical Theory of Finite Element Methods, Springer Science and Business Media

Cardona, A., Lozinski, A., Palacios, F., 2020, Finite element methods for computational fluid dynamics: A review, Journal of Computational Physics, 403, 109 066

Carlqvist, P., 1977, Currents in the solar atmosphere and a model for heating of the corona, Solar Physics, 55, 305–317

Celli, N., Burlini, L., Zollo, A., 1999, A high-resolution 3-d seismic model of the lithosphere and upper mantle beneath the central andes, Geophysical Research Letters, 26, 3493–3496

Centeno, R., Schou, J., Hayashi, K., Norton, A., Hoeksema, J. T., Liu, Y., Leka, K. D., Barnes, G., 2014, The Helioseismic and Magnetic Imager (HMI) Vector Magnetic Field Pipeline: Optimization of the Spectral Line Inversion Code, Sol. Phys., 289, 3531–3547, 1403.3677

Centeno, R., Milić, I., Rempel, M., Nitta, N. V., Sun, X., 2023, Limitations and biases in the retrieval of the polar magnetic field i: the role of the magnetic filling factor in milne-eddington inversions of simulated hinode/sp data, 2305.00924

Chen, Q., Liu, Y., Li, Y., Li, L., 2013, A global shallow-water model on yin-yang grids, International Journal of Geophysics, 2013, 1–13

Contopoulos, I., 2013, The Force-Free Electrodynamics Method for the Extrapolation of Coronal Magnetic Fields from Vector Magnetograms, Sol. Phys., 282, 419–426, 1209.5211

Contopoulos, I., Kalapotharakos, C., Georgoulis, M. K., 2011, Nonlinear force-free reconstruction of the global solar magnetic field: Methodology, Sol. Phys., 269, 351–365, 1011.5356

Courant, R., 1943, Finite elements and approximation, Journal of the Society for Industrial and Applied Mathematics, 2, 266–271

Cranmer, S. R., 2019, Solar wind: A review, Living Reviews in Solar Physics, 16, 4

Delaunay, B., 1934, Sur la sphre vide, Izvestiya Akademii Nauk SSSR. Otdelenie matematicheskikh i estestvennykh nauk, 7, 793–800

Dhiman, H. S., Gupta, A., 2020, Finite element analysis for heat transfer problems: A review, Journal of Thermal Science and Engineering Applications, 12, 041 003

Du, G., Chen, Y., Zhu, C., Liu, C., Ge, L., Wang, B., Li, C., Wang, H., 2018, Formation of Large-scale Coronal Loops Interconnecting Two Active Regions through Gradual Magnetic Reconnection and an Associated Heating Process, ApJ, 860, 40, `1805.04831`

Duchi, J., Hazan, E., Singer, Y., 2011, Adaptive subgradient methods for online learning and stochastic optimization, Journal of Machine Learning Research, 12, 2121–2159

Featherstone, N. A., Hindman, B. W., 2020, Solar convection zone: Structure and dynamics, Space Science Reviews, 216, 1–42

Feng, X., Jiang, C., Xiang, C., Zhao, X., Wu, S. T., 2012, A Data-driven Model for the Global Coronal Evolution, ApJ, 758, 62

Feng, X., Yang, L., Xiang, C., Jiang, C., Ma, X., Wu, S., Zhong, D., Zhou, Y., 2012, Validation of the 3d amr sip-cese solar wind model for four carrington rotations, Sol. Phys., 279, 207–229

Feng, X., Wang, H., Xiang, C., Liu, X., Zhang, M., Zhao, J., Shen, F., 2021, Magneto-hydrodynamic modeling of the solar corona with an effective implicit strategy, ApJS, 257, 34

Forveille, T., Shore, S., 2020, The Solar Orbiter mission, A&A, 642, E1

Gary, G. A., 2001, Plasma beta above a solar active region: Rethinking the paradigm, Sol. Phys., 203, 71–86

Gilat, A., Subramaniam, V., 2014, Numerical Methods for Engineers and Scientists: An Introduction with Applications using MATLAB, Wiley

Glatzmaier, G. A., 1987, Boundary element solutions of the potential equation for the solar corona, ApJ, 318, 485–493

Gosain, S., Pevtsov, A. A., Rudenko, G. V., Anfinogentov, S. A., 2013, First Synoptic Maps of Photospheric Vector Magnetic Field from SOLIS/VSM: Non-radial Magnetic Fields and Hemispheric Pattern of Helicity, ApJ, 772, 52, `1305.3294`

Gough, D. O., 2017, Solar radiation zone: some basics, Solar Physics, 292, 100

Gough, D. O., Thompson, M. J., 1988, The inversion problem for solar oscillations, Monthly Notices of the Royal Astronomical Society, 232, 259–283

Griffiths, D. J., 2017, Introduction to Electrodynamics, Cambridge University Press, 4th edn.

Guo, Q., Wang, X., Wang, Y., Ma, Z., 2019, Finite element methods for solving electromagnetic problems: A review of recent research, Progress in Electromagnetics Research M, 98, 1–22

Guo, Y., Ding, M. D., Liu, Y., Sun, X. D., DeRosa, M. L., Wiegelmann, T., 2012, Modeling Magnetic Field Structure of a Solar Active Region Corona Using Nonlinear Force-free Fields in Spherical Geometry, ApJ, 760, 47, `1210.0998`

Han, Z., Song, M. T., Fang, C., 2018, A finite-difference method for the solution of the coronal magnetic field model, MNRAS, 481, 2507–2516

Hestenes, M. R., Stiefel, E., 1952, Methods of conjugate gradients for solving linear systems, Journal of Research of the National Bureau of Standards, 49, 409–436

Holland, J. H., 1975, Adaptation in Natural and Artificial Systems, University of Michigan Press, Ann Arbor

Huang, W., Zhang, L., Zhang, Y., 2019, A review of unstructured mesh generation methods for computational fluid dynamics, Journal of Computational and Applied Mathematics, 345, 1–20

Inhester, B., Wiegelmann, T., 2006, Nonlinear Force-Free Magnetic Field Extrapolations: Comparison of the Grad Rubin and Wheatland Sturrock Roumeliotis Algorithm, Sol. Phys., 235, 201–221, `0801.3237`

Inoue, S., Magara, T., Pandey, V. S., Shiota, D., Kusano, K., Choe, G. S., Kim, K. S., 2014, Nonlinear force-free extrapolation of the coronal magnetic field based on the magnetohydrodynamic relaxation method, ApJ, 780, 101, `1311.3592`

Jiang, C., Feng, X., Xiang, C., 2012, A New Code for Nonlinear Force-free Field Extrapolation of the Global Corona, ApJ, 755, 62, `1206.1989`

Jing, J., Liu, C., Lee, J., Wang, H., 2013, Solar coronal magnetic field extrapolation using an eulerian remap of a non-linear force-free field on the yin-yang grid, The Astrophysical Journal, 777, 70

Jones, H. P., 1985, Recent studies of magnetic canopies, Australian Journal of Physics, 38, 919–928

Kageyama, A., Sato, T., 2004, "Yin-Yang grid": An overset grid in spherical geometry, Geochemistry, Geophysics, Geosystems, 5, Q09005, `physics/0403123`

Kageyama, M., Sato, T., Noda, A., Yoshimori, M., Yokoyama, C., Abe-Ouchi, A., Shigemitsu, M., Ohgaito, R., Takahashi, K., Komuro, Y., et al., 2004, A new generation of the gcm ocean-atmosphere model miroc, Advances in Atmospheric Sciences, 21, 289–302

Kennedy, J., Eberhart, R. C., 1995, Particle swarm optimization, in Proceedings of the IEEE International Conference on Neural Networks, vol. 4, pp. 1942–1948

Kirkpatrick, S., Gelatt Jr., C. D., Vecchi, M. P., 1983, Simulated annealing: A tool for operational research, Science, 220, 671–680

Klimchuk, J. A., 2015, Key aspects of coronal heating, Philosophical Transactions of the Royal Society of London Series A, 373, 20140256–20140256, `1410.5660`

Klimchuk, J. A., 2019, The physics of the solar chromosphere, Annual Review of Astronomy and Astrophysics, 57, 157–194

Koukras, A., Keppens, R., Dolla, L., 2022, Estimating uncertainties in the back-mapping of the fast solar wind, in EGU General Assembly Conference Abstracts, EGU General Assembly Conference Abstracts, pp. EGU22–10 570

Koumtzis, A., Wiegelmann, T., 2023, A New Global Nonlinear Force-Free Coronal Magnetic-Field Extrapolation Code Implemented on a Yin-Yang Grid, Sol. Phys., 298, 20

Kpyl, M. J., Korpi, M. J., Brandenburg, A., 2010, Numerical simulations of stellar convection with the eulag code on yin-yang grids, Astronomy & Astrophysics, 517, A44

Leighton, R. B., 1964, Transport of Magnetic Fields on the Sun., ApJ, 140, 1547

Leka, K. D., Barnes, G., Crouch, A. D., Metcalf, T. R., Gary, G. A., Jing, J., Liu, Y., 2009, Resolving the 180° Ambiguity in Solar Vector Magnetic Field Data: Evaluating the Effects of Noise, Spatial Resolution, and Method Assumptions, Sol. Phys., 260, 83–108

Lemen, J. R., Title, A. M., Akin, D. J., Boerner, P. F., Chou, C., Drake, J. F., Duncan, D. W., Edwards, C. G., Friedlaender, F. M., Heyman, G. F., Hurlburt, N. E., Katz, N. L., Kushner, G. D., Levay, M., Lindgren, R. W., Mathur, D. P., McFeaters, E. L., Mitchell, S., Rehse, R. A., Schrijver, C. J., Springer, L. A., Stern, R. A., Tarbell, T. D., Wuelser, J.-P., Wolfson, C. J., Yanari, C., Bookbinder, J. A., Cheimets, P. N., Caldwell, D., Deluca, E. E., Gates, R., Golub, L., Park, S., Podgorski, W. A., Bush, R. I., Scherrer, P. H., Gummin, M. A., Smith, P., Auker, G., Jerram, P., Pool, P., Soufli, R., Windt, D. L., Beardsley, S., Clapp, M., Lang, J., Waltham, N., 2012, The Atmospheric Imaging Assembly (AIA) on the Solar Dynamics Observatory (SDO), Sol. Phys., 275, 17–40

LeVeque, R. J., 2007, Finite Differences for Ordinary and Partial Differential Equations, Siam

Lionello, R., Velli, M., Downs, C., Linker, J. A., Miki, Z., Verdini, A., 2014, Validating a time-dependent turbulence-driven model of the solar wind, ApJ, 784, 120, `1402.4188`

Liu, Y., Lin, H., 2008, Observational test of coronal magnetic field models. i. comparison with potential field model, ApJ, 680, 1496–1507, `0710.3223`

Liu, Y., Hoeksema, J. T., Sun, X., Hayashi, K., 2017, Vector Magnetic Field Synoptic Charts from the Helioseismic and Magnetic Imager (HMI), Sol. Phys., 292, 29

Logan, D. L., 2017, A First Course in the Finite Element Method, Cengage Learning, 6th edn.

Low, B. C., Lou, Y., 1990, Modeling the formation of filament channels in the solar corona, The Astrophysical Journal, 352, 343–360

Low, B. C., Lou, Y. Q., 1990, Modeling Solar Force-free Magnetic Fields, ApJ, 352, 343

Loy, C. P., Liew, P. C., Rahman, M. M., 2020, Advancing front techniques and delaunay triangulation for mesh generation: A comparative review, Mathematics, 8, 329

Marsch, E., 2006, Kinetic physics of the solar corona and solar wind, Living Reviews in Solar Physics, 3, 1

McLaughlin, J. A., 1989, Finite element analysis of the potential field in the solar corona, Sol. Phys., 123, 41–56

Metcalf, T. R., 1994, Resolving the 180-degree ambiguity in vector magnetic field measurements: The 'minimum' energy solution, Sol. Phys., 155, 235–242

Metcalf, T. R., Leka, K. D., Barnes, G., Lites, B. W., Georgoulis, M. K., Pevtsov, A. A., Balasubramaniam, K. S., Gary, G. A., Jing, J., Li, J., Liu, Y., Wang, H. N., Abramenko, V., Yurchyshyn, V., Moon, Y. J., 2006, An Overview of Existing Algorithms for Resolving the 180 Ambiguity in Vector Magnetic Fields: Quantitative Tests with Synthetic Data, Sol. Phys., 237, 267–296

Mikic, Z., McClymont, A. N., 1994, Deducing coronal magnetic fields from vector magnetograms, in Solar Active Region Evolution: Comparing Models with Observations, (Eds.) K. S. Balasubramaniam, G. W. Simon, vol. 68 of Astronomical Society of the Pacific Conference Series, p. 225

Mou, C., Madjarska, M. S., Galsgaard, K., Xia, L., 2018, Eruptions from quiet Sun coronal bright points. I. Observations, A&A, 619, A55, `1808.04541`

Nesterov, Y., 1983, A method for solving the convex programming problem with convergence rate $o(1/k^2)$, Doklady AN SSSR, 269, 543–547

Nocedal, J., Wright, S. J., 2006, Numerical Optimization, Springer, 2nd edn.

Pedregal, P., 2004, Introduction to Optimization, Springer

Pesnell, W. D., Thompson, B. J., Chamberlin, P. C., 2012, The Solar Dynamics Observatory (SDO), Sol. Phys., 275, 3–15

Petrie, G. J. D., 2000, Three-dimensional Equilibrium Solutions to the Magnetohydrodynamic Equations and their Application to Solar Coronal Structures, Ph.D. thesis, Department of Mathematics and Statistics, University of St. Andrews, North Haugh, St Andrews KY16 9SS

Robbins, H., Monro, S., 1951, A stochastic approximation method, The annals of mathematical statistics, 22, 400–407

Ruffert, P. M., 2014, Numerical Methods for Astrophysics: An Introduction, Wiley-VCH, 2nd edn., ISBN 978-3-527-40995-1

Sakurai, T., 1981, Calculation of force-free magnetic field with non-constant , Solar Physics, 69, 343–359

Schatten, K. H., Wilcox, J. M., Ness, N. F., 1969, A model of interplanetary and coronal magnetic fields, Sol. Phys., 6, 442–455

Scherrer, P. H., Schou, J., Bush, R. I., Kosovichev, A. G., Bogart, R. S., Hoeksema, J. T., Liu, Y., Duvall, T. L., Zhao, J., Title, A. M., Schrijver, C. J., Tarbell, T. D., Tomczyk, S., 2012, The Helioseismic and Magnetic Imager (HMI) Investigation for the Solar Dynamics Observatory (SDO), Sol. Phys., 275, 207–227

Schrijver, C. J., De Rosa, M. L., Metcalf, T. R., Liu, Y., McTiernan, J., Régnier, S., Valori, G., Wheatland, M. S., Wiegelmann, T., 2006, Nonlinear Force-Free Modeling of Coronal Magnetic Fields Part I: A Quantitative Comparison of Methods, Sol. Phys., 235, 161–190

Shewchuk, J. R., 1996, Triangle: engineering a 2d quality mesh generator and delaunay triangulator, Applied Computational Geometry: Towards Geometric Engineering, pp. 203–222

Shibata, K., Magara, T., 2011, Solar flares: Magnetohydrodynamic processes, Living Reviews in Solar Physics, 8, 6

Skamarock, W. C., Klemp, J. B., 1997, Multigrid techniques for weather forecasting models on unstructured meshes, Monthly Weather Review, 125, 1358–1371

Song, M. T., Fang, C., Zhang, H. Q., Tang, Y. H., Wu, S. T., Zhang, Y. A., 2007, Reconstructing Spherical Nonlinear Force-free Field in the Solar Corona, ApJ, 666, 491–500

Stix, M., 2004, The Sun: An Introduction, Springer, 2nd edn., ISBN 978-3-540-22370-1

Sun, W., Han, L., Li, J., 2011, The polar fourier transform and singular value decomposition methods for atmospheric corrections of gravity data, Journal of Geodesy, 85, 637–648

Sutskever, I., Martens, J., Dahl, G., Hinton, G., 2013, On the importance of initialization and momentum in deep learning, in Proceedings of the 30th International Conference on Machine Learning (ICML-13), pp. 1139–1147

Svalgaard, L., Duvall, Jr., T. L., Scherrer, P. H., 1978, The strength of the sun's polar fields, Sol. Phys., 58, 225–239

Tadesse, T., Wiegelmann, T., Inhester, B., 2009, Nonlinear force-free coronal magnetic field modelling and preprocessing of vector magnetograms in spherical geometry, A&A, 508, 421–432, `0912.1514`

Tadesse, T., Wiegelmann, T., Inhester, B., Pevtsov, A., 2011, Nonlinear force-free field extrapolation in spherical geometry: improved boundary data treatment applied to a SOLIS/VSM vector magnetogram, A&A, 527, A30, `1011.6285`

Tadesse, T., Wiegelmann, T., Gosain, S., MacNeice, P., Pevtsov, A. A., 2014, First use of synoptic vector magnetograms for global nonlinear, force-free coronal magnetic field models, A&A, 562, A105, `1309.5853`

Thanasoulis, E., Kazachenko, M. D., MacNeice, P. J., Lionello, R., 2020, Non-linear force-free coronal magnetic field extrapolation on a spherical grid, Astronomy & Astrophysics, 640, A75

Tian, H., 2018, The solar transition region, Living Reviews in Solar Physics, 15, 4

Tomczyk, S., McIntosh, S. W., Keil, S. L., Judge, P. G., Schad, T., Seeley, D. H., Edmondson, J., 2007, Alfvn waves in the solar corona, Science, 317, 1192

Tóth, G., van der Holst, B., Huang, Z., 2011, Obtaining potential field solutions with spherical harmonics and finite differences, ApJ, 732, 102, `1104.5672`

Usmanov, A. V., 1996, Magnetic fields and plasma processes in the heliosphere, in American Institute of Physics Conference Series, (Eds.) D. Winterhalter, J. T. Gosling, S. R. Habbal, W. S. Kurth, M. Neugebauer, vol. 382 of American Institute of Physics Conference Series, pp. 141–144

Valori, G., Kliem, B., Keppens, R., 2005, Extrapolation of a nonlinear force-free field containing a highly twisted magnetic loop, A&A, 433, 335–347

Valori, G., Kliem, B., Fuhrmann, M., 2007, Magnetofrictional Extrapolations of Low and Lou's Force-Free Equilibria, Sol. Phys., 245, 263–285

Wang, J., Ao, X., Wang, Y., Wang, C., Cai, Y., Luo, B., Liu, S., Shen, C., Zhuang, B., Xue, X., Gong, J., 2018, An operational solar wind prediction system transitioning fundamental science to operations, Journal of Space Weather and Space Climate, 8, A39

Wang, Q., Danilov, S., Sidorenko, D., Wekerle, C., Wang, F., Jung, T., 2014, The fesom2.0 model and its performance on the yin-yang grid, Geoscientific Model Development, 7, 2077–2096

Wheatland, M. S., Sturrock, P. A., Roumeliotis, G., 2000, An Optimization Approach to Reconstructing Force-free Fields, ApJ, 540, 1150–1155

Wheatland, M. S., Sturrock, P. A., Roumeliotis, G., 2000, An optimization approach to reconstructing force-free fields, ApJ, 540, 1150–1155

Wiegelmann, T., 2004, Optimization code with weighting function for the reconstruction of coronal magnetic fields, Sol. Phys., 219, 87–108, `0802.0124`

Wiegelmann, T., 2007, Nonlinear force-free modeling of the solar magnetic field, Sol. Phys., 240, 227

Wiegelmann, T., 2007, Computing Nonlinear Force-Free Coronal Magnetic Fields in Spherical Geometry, Sol. Phys., 240, 227–239, `astro-ph/0612124`

Wiegelmann, T., Inhester, B., 2010, How to deal with measurement errors and lacking data in nonlinear force-free coronal magnetic field modelling?, A&A, 516, A107

Wiegelmann, T., Neukirch, T., 2002, Including stereoscopic information in the reconstruction of coronal magnetic fields, Sol. Phys., 208, 233–251, `0801.3234`

Wiegelmann, T., Sakurai, T., 2021, Solar force-free magnetic fields, Living Reviews in Solar Physics, 18, 1, `1208.4693`

Wiegelmann, T., Thalmann, J. K., Inhester, B., Tadesse, T., Sun, X., Hoeksema, J. T., 2012, How Should One Optimize Nonlinear Force-Free Coronal Magnetic Field Extrapolations from SDO/HMI Vector Magnetograms?, Sol. Phys., 281, 37–51, `1202.3601`

Wiegelmann, T., Neukirch, T., Nickeler, D. H., Chifu, I., 2020, An optimization principle for computing stationary mhd equilibria with solar wind flow, Sol. Phys., 295, 145, `2010.02945`

Williamson, D. L., Drake, J. B., 2003, A new global shallow-water model with a staggered grid, Journal of Climate, 16, 691–707

Worden, J., Harvey, J., 2000, An Evolving Synoptic Magnetic Flux map and Implications for the Distribution of Photospheric Magnetic Flux, Sol. Phys., 195, 247–268

Wu, S. T., Sun, M. T., Chang, H. M., Hagyard, M. J., Gary, G. A., 1990, On the numerical computation of nonlinear force-free magnetic fields, ApJ, 362, 698

Yan, Y., Sakurai, T., 2000, New boundary integral equation representation for finite energy force-free magnetic fields in open space above the sun, Sol. Phys., 195, 89–109

Yang, Q., Li, W., Xu, J., 2021, Finite volume method for electromagnetic simulation: A comprehensive review, IEEE Transactions on Magnetics, 57, 1–18

Yeates, A. R., Amari, T., Contopoulos, I., Feng, X., Mackay, D. H., Mikić, Z., Wiegelmann, T., Hutton, J., Lowder, C. A., Morgan, H., Petrie, G., Rachmeler, L. A., Upton, L. A., Canou, A., Chopin, P., Downs, C., Druckmüller, M., Linker, J. A., Seaton, D. B., Török, T., 2018, Global Non-Potential Magnetic Models of the Solar Corona During the March 2015 Eclipse, Space Sci. Rev., 214, 99, `1808.00785`

Yeates, A. R., Cheung, M. C. M., Jiang, J., Petrovay, K., Wang, Y.-M., 2023, Surface Flux Transport on the Sun, arXiv e-prints, arXiv:2303.01209, `2303.01209`

Young, D. M., 1950, Iterative Methods for Solving Partial Difference Equations of Elliptic Type, Ph.D. thesis, Harvard University, Cambridge, MA, USA

Yu, W., Jin, J.-M., 2017, Finite Volume Methods for Electromagnetic Field Modeling, Morgan & Claypool Publishers, ISBN 978-1627058203

Zhao, J., Cai, C., Wei, X., 2022, A review of delaunay-based methods for numerical simulation of complex geometries, Applied Mathematical Modelling, 100, 111–132

Zhu, X., Neukirch, T., Wiegelmann, T., 2022, Magnetohydrostatic modeling of the solar atmosphere, arXiv e-prints, arXiv:2203.15356, `2203.15356`

Publications

Refereed publications

- Argyrios Koumtzis and Thomas Wiegelmann (2023). "A New Global Nonlinear Force-Free Coronal Magnetic-Field Extrapolation Code Implemented on a Yin-Yang Grid". Solar Physics, 298(2), p.20. DOI: 10.1007/s11207-023-02109-6.

Conference talks and posters

- Talk - Argyrios Koumtzis and Thomas Wiegelmann (2022). "A new global nonlinear force-free coronal magnetic-field extrapolation code implemented on a Yin Yang grid." EGU General Assembly Conference Abstracts. DOI: 10.5194/egusphere-egu22-11960.

- Talk - Koumtzis, A., Wiegelmann, T., and Madjarska, M.: Computing the global coronal magnetic field during activity maximum and minimum with a newly developed nonlinear force-free Yin-Yang code, EGU General Assembly 2023, Vienna, Austria, 24–28 Apr 2023, EGU23-17168, https://doi.org/10.5194/egusphere-egu23-17168, 2023.

Acknowledgements

First and foremost, I wish to extend my deepest gratitude to Prof Dr Sami Solanki for his unwavering belief in my abilities and his instrumental role in launching my PhD journey at MPS. His faith in my potential convinced the University of Göttingen to endorse my direct admission to the PhD program, bypassing the traditional requirement of a master's degree. His ability to acknowledge and appreciate my efforts not only provided me with an incredible opportunity but also ignited my passion for this project.

In the same breath, I cannot overlook the immense contribution of my supervisor, Dr Thomas Wiegelmann, to the successful completion of this project. His astute understanding of code development, combined with his incredible patience during those challenging periods when I could not produce immediate results due to coding bugs, were nothing short of invaluable. Thomas never once faltered in his trust in me or the potential success of our project, even when faced with obstacles before the validation of my model. He continuously offered encouragement and motivation, ensuring my focus remained on the overarching goals of the project. Having a supervisor endowed with such technical prowess and, more importantly, responsiveness that transcended traditional working hours, truly catalyzed my progress. This accessibility not only reduced potential frustration but also maintained it at a healthy level, which was integral to my overall learning and growth throughout this journey. So, Thomas thank you again for everything and I hope we can continue working together in the future.

I must also express my deep appreciation for Prof Hardi Peter, whose guidance and support remained consistent throughout my journey. Although he was not directly involved in the technical aspects of the project, his advice on navigating the intricate maze of a PhD was a beacon of enlightenment. His wisdom was truly invaluable in successfully treading the path of this challenging endeavor.

Equally, my heartfelt gratitude extends to Dr Maria Madjarska for her persistent guidance, unwavering support, and consistent encouragement. Together, we toiled over the manuscript of my first paper, refining each minute detail to reach perfection. We achieved our goal and had our work accepted within a week, requiring only minor corrections. The success of this feat is testament to Maria's dedication and mentorship. Thank you, Maria, for your faith in my abilities and your ongoing effort to help me secure a promising career.

I wish to express my profound gratitude to Dr. Bernd Inhester. Our enlightening discussions about numerical methods and optimization algorithms have significantly contributed to my research and understanding. Your wisdom and comprehensive knowledge in these areas are unparalleled, and I am immensely grateful for the privilege of learning from you. Your willingness to delve into these intricate topics and your ability to elucidate them with such clarity reflects a deep mastery only achievable through a strong command and understanding of the subject matter. So, thank you once again, Dr. Inhester, for being

ever ready to share your insights, for explaining complex concepts with adeptness, and for fostering my growth in this fascinating field.

Family, the cornerstone of my journey, deserve more than just a passing mention. My parents, despite lacking specific expertise in my field, have taken an active interest in my project. Their curiosity has provided me with the unique opportunity to explain my research in a relatable manner to the general public, keeping me grounded and in touch with the real world. A special note of thanks goes to my mother, whose unwavering support was apparent when she spent two months in Göttingen, helping me find a new home and organize it from scratch after an unfortunate flooding incident. My father was also always there a source of optimism humor and motivation. They both never stopped believing that I would manage to finish my project getting the best possible results.

My gratitude extends to my friends who transformed the rigors of this PhD journey into a memorable and wonderful experience. Our shared moments in restaurants, coffee breaks, and numerous social activities added an indelible hue to my doctoral studies. Amanda Romero, Tanayveer Vhatia, and Dusan Vukadinovic, your support was unquantifiable. From moving into my new house, to assembling furniture, to assisting with the paperwork for my disability card, your help was boundless. I can't imagine navigating this journey without your presence.

Our office, enlivened by Tanayveer and Dusan, was more than just a workspace. It was a realm filled with camaraderie, jokes, and leisure, perhaps even more than actual work. We shared our dreams and our fears for the future. The celebration of every small achievement fostered a sense of community that was immensely comforting. I am eternally grateful and can only hope that my future workplaces host such a welcoming and uplifting atmosphere. At this juncture, that notion seems quite challenging to match. Thank you, my friends, for making this journey an unforgettable one. I would like to express my heartfelt appreciation to Amanda Romero for our culinary escapades throughout Germany, Greece, and the Netherlands. These experiences have undoubtedly infused my PhD journey with some of the most unforgettable flavors and remarkable memories.

To my dear friend Jesper Tjoa, I extend my sincerest gratitude. You have been the glue that bonded us all, becoming the very essence of our friendship. Your dynamic energy, infectious humor, and tireless efforts to make each day unique and engaging have truly left an indelible mark. It's your thoughtful and profound conversations that have enriched us, propelling us towards becoming better versions of ourselves.

I am profoundly grateful to you, Philipp Löschl, for our extensive discussions that encompassed both data-centric subjects and those that transcended the realm of data. I appreciate you introducing me to exceptional resources that have greatly contributed to my wellness and productivity. I extend my thanks for your willingness to read letters, assist in the supermarket, and perform numerous other small acts of kindness that have made my life much much easier.

Jonas Sinjan my friend, thank you for sharing your expertise regarding the reliability of polar data. Thank you also for for being a so cool and fun. I enjoyed our conversations about fitness, investments and sports. So thank you again Iron Man.

I would like to extend my heartfelt thanks to Paula Wulff. Your multifaceted assistance, from accompanying me to the EGU conference in Vienna to adeptly navigating the labyrinth of bureaucracy, has been indispensable. I am truly grateful for your invaluable support. Furthermore, you exemplify an admirable balance between professional and

personal life. Not only are you an exceptional scientist, but you also maintain a robust commitment to sports, serving as a source of inspiration and motivation for those around you. Thank you, Paula, for being such an incredible role model and for demonstrating that it is indeed possible to excel in our chosen fields while also making time for physical health and wellbeing.

My friend, Nikolina. Your generous contribution to my work, through sharing scripts to download and query data, has been indispensable. Your willingness to painstakingly explain the workings of each procedure saved me an immeasurable amount of time and effort, thus streamlining my research process and greatly facilitating my PhD journey. Additionally, our discussions about navigating PhD supervision have been incredibly helpful. Beyond our professional collaboration, I cherish the moments of camaraderie we've shared. Your delightful cakes and cookies, always prepared with love and shared generously, added a touch of warmth and sweetness to our PhD experience. Thank you, Nikolina, not just for your friendship and your professional guidance, but also for the meaningful contributions that have made this journey all the more memorable.

I extend my heartfelt gratitude to Neelanchal Joshi. Our dialogues about machine learning and AI have been profoundly illuminating. Your knack for elucidating complex concepts with remarkable clarity and proficiency has greatly augmented my understanding of these areas. Your tendency to incorporate fresh dimensions, both physical and metaphorical, into our discussions has broadened my perspective and challenged my thinking. You have a unique gift for taking concepts beyond their typical boundaries, adding an enriching depth to my worldview. Beyond your academic input, your vibrant humor and infectious energy have made our interactions a source of joy and inspiration. Thank you, Neelanchal, for your intellectual contributions, your lively spirit, and the positive atmosphere you consistently foster.

I would like to express my deepest gratitude to my friend, Sanghita Chandra. Our philosophical dialogues have enriched our understanding of life's intricacies and left an indelible mark on my thinking. In addition to these mind-expanding conversations, I must thank you for the incredible Indian cuisine that you generously shared with me. Your unwavering presence and support during my moments of crisis were invaluable. You've been an empathetic listener, making space for my grievances and responding with kindness. For all of these reasons, I sincerely thank you, Sanghita.

To Proutpitos Dei, my cherished gym companion and co-conspirator, I am grateful for your camaraderie. You hold the unique distinction of being the only person in the institute with a sense of humor that outshines even mine. Our memorable puns should echo through the annals of history, eternally testifying to our shared brilliance. Your presence added an element of joy and levity during the challenging months of thesis writing, and even our unsuccessful attempts at cutting and bulking became cherished memories. Your contribution to making life more enjoyable is truly invaluable.

I wish to extend my deepest gratitude to my partner, Constanze. You have been an unwavering companion throughout this doctoral journey, infusing every day with brightness and a sense of joy that transformed even the most arduous tasks into bearable challenges. Your unflinching support, both emotional and intellectual, has been a linchpin in my ability to navigate this taxing endeavour. I am deeply thankful for the patience you displayed amidst the academic pressures and for sharing the stress that often accompanied the unexpected twists and turns of my PhD journey. Your continuous encouragement has been an

invaluable source of motivation, a beacon guiding me through periods of self-doubt and uncertainty. The German wisdom you've shared, particularly your reminders to tackle challenges step by step kept me on track. Whenever I faltered or felt overwhelmed, you were there to assure me that everything would eventually come together, and that perseverance and tenacity would eventually lead to success. Thank you, Constanze, for being not just my partner, but my guide, my pillar of strength, and my constant source of inspiration throughout this demanding yet rewarding journey.

I want to thank so many people at the MPS that have been so welcoming and helpful to make this research institute not a work place but my real house in Germany.

Curriculum vitae

Name: Argyrios Sotirios Koumtzis
Date of Birth: 22.01.1996
Place of Birth: Thessaloniki, Greece

Education:
Oct 2019 - July 2023
PhD
International Max Planck Research School (IMPRS) at Max Planck Institute for Solar System Research (MPS) and University of Göttingen, Germany

Oct 2014 - Oct 2019
Bachelor in physics(BSC)
Aristotle University of Thessaloniki, Thessaloniki, Greece
Grade 9.39/10 (top 1%)